ENHANCEMENT OF TRAJECTORY FOLLOWING ACCURACY OF HIGH ACCELERATION ROBOTS BY USING THEIR STIFFNESS PROPERTIES

A Thesis Submitted to
the Graduate School of Engineering and Sciences of
İzmir Institute of Technology
in Partial Fulfillment of the Requirements for the Degree of

MASTER OF SCIENCE

in Mechanical Engineering

by
Erkan PAKSOY

December 2021
İZMİR

dedicated to my parents Ayşegül and Sabri PAKSOY.

ACKNOWLEDGMENTS

First of all, I would like to thank my supervisor Dr. M.İ. Can Dede for his patience, guidance and endless support during my thesis studies. I also would like to thank Dr. Gökhan Kiper and Dr. M.İ. Can Dede for giving me a chance work in their project and contributions in parts of this study.

I would like to thank the members of Modelling and Prototyping Laboratory, Human-Robot Interaction Laboratory, Robotics Laboratory and Rasim Alizade Mechatronics Laboratory.

I am thankful to Dr. Emre Uzunoğlu and Mr. İbrahimcan Görgülü for their reasonable and well-considered suggestions that assisted in the accomplishment of this thesis study.

I am eternally grateful to my family (Mr. Sabri Paksoy, Mrs. Ayşegül Paksoy, and Mrs. Esma Paksoy) for constantly encouraging me to study and making sacrifices for my education.

I would like to especially thank to my friends who were or were not with me during the thesis but are essential individuals in my life: Ms. Perimsu Gürboğa, Mrs. Ceylin Kızılkaya, Mr. Can Genç.

Probably, it is not the appropriate place but is a good opportunity for me to express my gratitude to the Ms. Hazal Emet. With her, I shared so many great moments. She is deserving of the best.

I would also like to thank Mr. Kubilay Yıldırım and IPG Photonics Eurasia for delivering the laser process head with its subsystems.

This study is supported in part by The Scientific and Technological Research Council of Turkey (TÜBİTAK) via grant number 116M272 and entitled ”Methodologies for Increasing the Positioning Accuracy of High-Acceleration Parallel Robots Used in Industrial Applications”.

ABSTRACT

ENHANCEMENT OF TRAJECTORY FOLLOWING ACCURACY OF HIGH ACCELERATION ROBOTS BY USING THEIR STIFFNESS PROPERTIES

In recent years, there has been a push for the incorporation of robots into manufacturing processes. In general, parallel robots are preferred for processes requiring high repeatability and positioning accuracy. If the positioning accuracy of the end-effector of a robot has high priority, compliance characteristics of the elements of its mechanism should be considered. Due to the high accelerations or external loading on the robot, the dimensions of the elements change and this leads to positioning errors for the end-effector.

This thesis describes an experimental test setup and an experimental procedure for determining the compliance characteristics of planar mechanisms, followed by a comparison of the repeatability and stiffness performance of a parallel and an over-constrained mechanism. Finally, assumptions and methodology for using this compliance information to improve the trajectory tracking accuracy of high-accelerated robots are given.

Portable coordinate measurement machine and calibrated weights are used to collect compliance information. The compliance behavior of the mechanisms defined for entire workspace by using the least squares and bilinear interpolation techniques. The D'Alambert principle is used to estimate fictitious forces that cause the compliance of the mechanism's end-effector while the mechanism operates at up to 5 g accelerations.

As a result of this thesis, it is demonstrated that the mechanism's center of gravity and joint types play an important role in the mechanism's trajectory tracking accuracy, and that tracking accuracy can be improved by a simple data-driven compliance prediction algorithm.

ÖZET

YÜKSEK İVMELİ ROBOTLARIN DİRENGENLİK ÖZELLİKLERİ KULLANILARAK YÖRÜNGE TAKİP HASSASİYETLERİNİN İYİLEŞTİRİLMESİ

Son yıllarda, robotların üretim süreçlerine dahil edilmesi yönünde bir eğilim bulunmaktadır. Genel olarak, yüksek tekrarlanabilirlik ve konumlama hassasiyeti gerektiren işlemler için paralel robotlar tercih edilir. Bir robotun uç noktasının konumlandırma hassasiyeti yüksek önceliğe sahipse, robotta kullanılan elemanların direngenlik özellikleri dikkate alınmalıdır. Robot üzerindeki yüksek ivmeler veya dış kuvvetler nedeniyle, elemanların boyutları değişebilir ve bu durum robotun uç noktasında konumlandırma hatalarına sebep olur.

Bu tez, düzlemsel mekanizmaların direngenlik özelliklerini belirlemek için deneysel bir test düzeneği ve deneysel bir prosedürü, ardından paralel ve aşırı kısıtlı bir mekanizmanın tekrarlanabilirlik ve direngenlik performansının bir karşılaştırmasını ve son olarak bu direngenlik bilgilerinin yüksek ivmeli robotların yörünge izleme doğruluğunun iyileştirilmesinde kullanılması için varsayımları ve metodolojiyi açıklar.

Direngenlik ya da esneklik bilgilerini toplamak için Faro Prime Arm ve kalibre edilmiş ağırlıklar kullanılır. En küçük kareler yöntemi ve çift yönlü doğrusal enterpolasyon teknikleri kullanılarak tüm çalışma alanı için mekanizmanın esneme bilgisi elde edilmiştir. D'Alambert ilkesi, mekanizma 5 g yer çekimi ivmelerine kadar hareket ederken, mekanizmanın uç noktasının esnemesinin hangi kuvvetler sonucunda olduğunu tahmin etmek için kullanılır.

Bu tez sonucunda, mekanizmanın ağırlık merkezi ve eklem tiplerinin, mekanizmanın yörünge izleme doğruluğunda önemli bir rol oynadığı ve izleme doğruluğunun basit bir veriye dayalı esneme tahmin algoritması ile iyileştirilebileceği gösterilmiştir.

TABLE OF CONTENTS

LIST OF FIGURES

LIST OF TABLES

CHAPTER 1

INTRODUCTION

1.1. Motivation

In 2012, a SANTEZ (Industrial Theses Support Program) Project called ”Kinematically Redundant Laser Cutting Machine Designed” was started. The primary purpose of the SANTEZ Project was to use the MMM (Macro-Micro Manipulation) idea to shorten the duration of the operation performed by a conventional size planar laser-cutting machine. The crucial aspect is that not only should the operation time be reduced, but the positioning accuracy and repeatability should also be enhanced when designing the machine. In this project, the positioning accuracy is determined using the standard VDI/DGQ 3441 - Statistical Testing of the Operational and Positional Accuracy of Machine Tools; Basis. In this standard, the positioning accuracy is related to a function of the measured length of trajectory. However, trajectory accuracy or dynamic performance of the machine should be considered. In the SANTEZ Project, it is shown that the dynamic performance of the designed system should be improved (Uzunoğlu, 2019).

As a result, a TUBİTAK Project called ”Methodologies for Increasing the Positioning Accuracy of High-Acceleration Parallel Robots Used in Industrial Application” was started in 2017. This project focus on increasing the positioning accuracy of the micro-manipulator of the designed machine in SANTEZ Project which is an over-constrained mechanism. In the TUBİTAK Project, there are mainly three subjects: static calibration, dynamic balancing, and stiffness modeling of the mechanism to increase the positioning accuracy. Static calibration is about increasing the positioning accuracy of a mechanism in static condition. The dynamic balancing process aims to decrease the vibrations by preventing the forces exerted on the fixed base. The stiffness modeling of the mechanism can increase trajectory tracking of the end-effector by estimating the compliance of the mechanism.

This thesis is based on the stiffness modeling part of the TUBİTAK Project. The aim is to enhance the trajectory tracking accuracy of high acceleration robots by using their stiffness properties. Another aim is to investigate the dynamic performance of the

mechanism by considering deviations from the linearity that is not stated in the standard.

1.2. Outline

Chapter 2 is an introductory chapter that starts with an overview of some important factors in robotic applications and indicates that analyzing a robot's compliance is critical in high-accelerated operations. Following that, it provides examples of compliance measurement techniques. After that, it gives a similar methodology for measuring an over-constrained mechanism's compliance information in order to be used in high-accelerated operation. Finally, it presents validation of the methodology by evaluating the compliance values of the mechanism at symmetric configurations.

Chapter 3 gives brief information about serial, parallel and over-constrained mechanisms. After that, by using the verified experimental measurement procedure, a comparison study in terms of stiffness characteristics and repeatability between two kinematically equivalent mechanisms (a parallel mechanism and the over-constrained mechanism indicated at the previous chapter) is presented.

In Chapter 4, data-driven compliance modeling to enhance trajectory following of high acceleration robots by presenting its assumptions, methodology, and novelty are given. The system's hardware and software are introduced. Also, the effect of the center of gravity location and the compliance model on the trajectory following performance of the mechanisms are demonstrated. Moreover, an image processing based trajectory tracking capability comparison is conducted between the defined mechanisms in order to show that how changes trajectory tracking ability between these mechanisms in terms of some defined performance metrics.

Chapter 5 gives brief summary and presents findings and outcomes of the studies. Schematic of the outline can be seen in Figure 1.1 as a summary. OC is an abbreviation for 2-degrees-of-freedom over-constrained planar mechanism, whereas SC is an abbreviation for 2-degrees-of-freedom simply-constrained planar mechanism. CAD models of the mechanisms are given in 3.1.

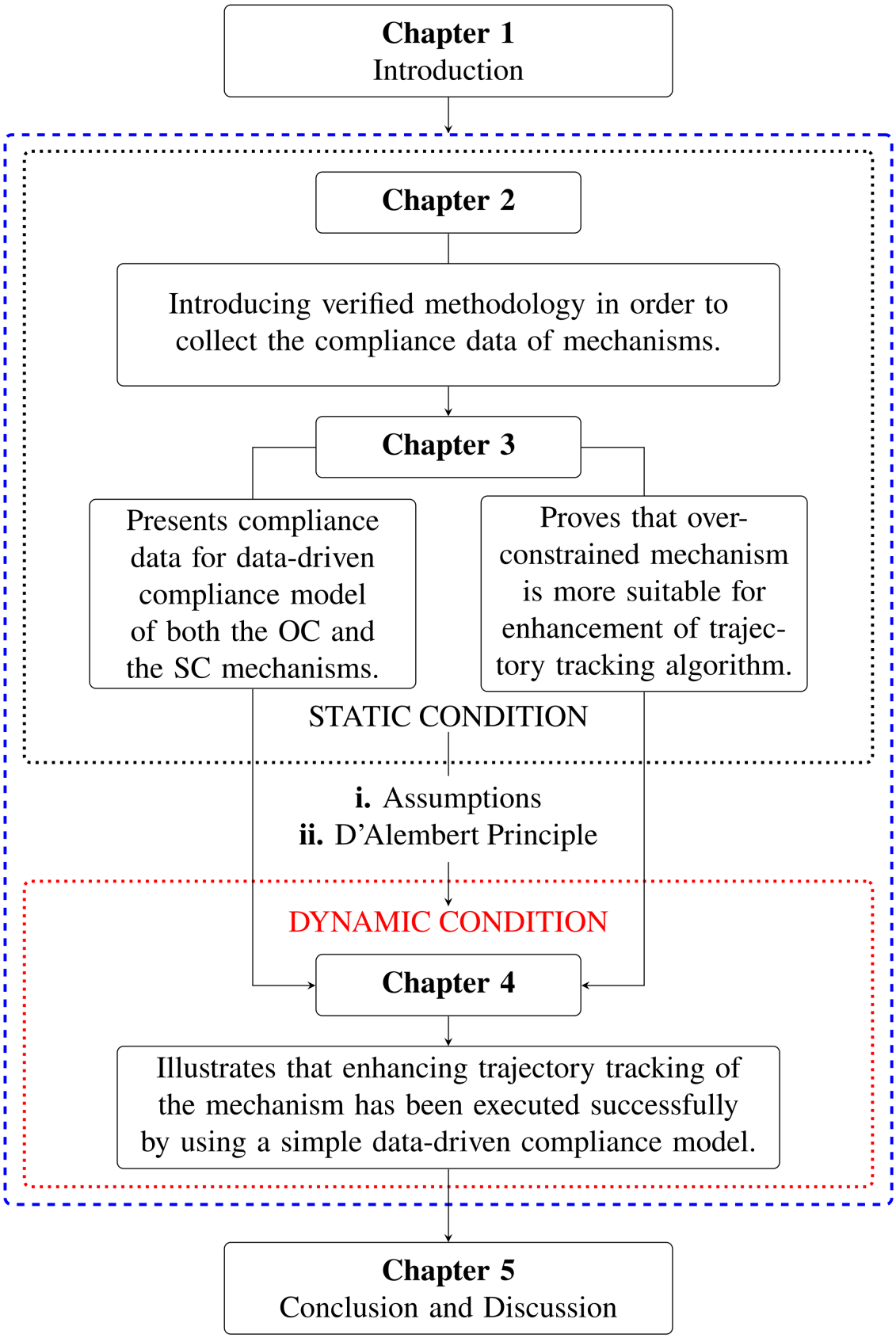

Figure 1.1. Schematic of the Outline

CHAPTER 2

EXPERIMENTAL COMPLIANCE MATRIX DERIVATION

2.1. Introduction

In order to express the positioning performance of a robotic manipulator, commonly the resolution, repeatability and accuracy of the robot are considered. The resolution is defined as the smallest incremental step that the robot's end-effector can move, and it mostly depends on the actuator and sensor capabilities. Repeatability is defined as the robot's ability to return to the same position and orientation. Accuracy is a measure of how accurately the robot can move to a desired location in workspace (Conrad et al., 2000).

Factors that affect the accuracy of a robotic manipulator named as inaccuracy factors and classified into two groups as geometrical errors and non-geometrical errors. Geometrical errors are due to three factors: manufacturing tolerances, assembly process and joint clearance. On the other hand, non-geometrical errors can be categorized into 5 subgroups which are compliance errors, measurement errors, environmental factors (temperature, humidity), control errors and the final one is the problems caused in the joint structure: friction, backlash and wear (Klimchik, 2011).

All 3 subgroups in the geometrical factors affect the accuracy of the robot and joint clearance errors have a dominant effect on the repeatability of the robot. By various calibration methods, the accuracy problems can be solved. To enhance the repeatability of a robot, an over-constrained kinematic structure can be used so that the effect of the joint clearances is reduced. Over-constrained mechanisms have lower computed degrees of freedom (DoF) than practical degrees of freedom (Gogu, 2005).

In this chapter, we want to focus on how compliance information of the end-effector point can be obtained for a 2-DoF over-constrained planar parallel manipulator. Here, we assume that the other non-geometrical factors have small effect on the end-effector position compared to the effect of the compliance errors. The reason of assuming compliance errors have dominant effect on the end-effector location is that the mechanism includes links manufactured as a combination of aluminum parts and carbon fiber tubes

connected to each other by glue and the end-effector accelerations are up to 5 g.

In order to determine the Cartesian compliance matrix or stiffness matrix of the manipulator, there are two methods classified as analytical and experimental stiffness modeling methods. In this chapter, an experimental stiffness modeling method is described and the results of the experiments are presented for a 2-DoF over-constrained planar mechanism.

In experimental stiffness evaluation systems, generally the system consists of 2 elements; one of them is the displacement measurement sensor and the other one is the calibrated masses to create different set of force matrices. In an example experimental method, a formulation for numerical and experimental stiffness analysis and basic principles on how the stiffness matrix of a manipulator can be obtained experimentally are given. In a previous study, an experimental stiffness measuring system called Milli-CATRASYS system was produced to procure the stiffness characteristics of a parallel manipulator called CaPaMan. This system includes LVDT sensors on the steel wires in order to measure the end-effector displacements and calibrated masses on the end of each wire to create different set of force matrices (Ceccarelli and Carbone, 2005).

In another experimental stiffness measurement method, a measurement system composed of cameras is used to measure the end-effector displacements of a haptic device (Taner and Dede, 2017).

Alici and Shirinzadeh (2005), used a laser tracker and reflector system in order to measure the end-effector pose and a force sensor is used to ensure the direction and magnitude of the force. In this thesis, Faro Prime Measuring Arm 1.2 is used as the displacement measuring element and calibrated masses are used via a wire-pulley system to create different forces at the end-effector of a 2-DoF over-constrained mechanism designed for planar laser marking operation with high acceleration motion capability. The aim of this chapter is to obtain compliance information of the end-effector by applying a variety of forces at various locations of its workspace. Then, in Chapter 4, this compliance data is used for compliance modeling of the mechanism, which is integrated into the trajectory planning procedure to enhance trajectory tracking accuracy of the mechanism.

2.2. 2-DoF Planar Over-constrained Mechanism

The two mechanisms presented in Figure 2.1a and 2.1b are kinematically equivalent when the positioning of point C is of concern given that the corresponding link lengths are equal to each other, assuming that links and joints are rigid.

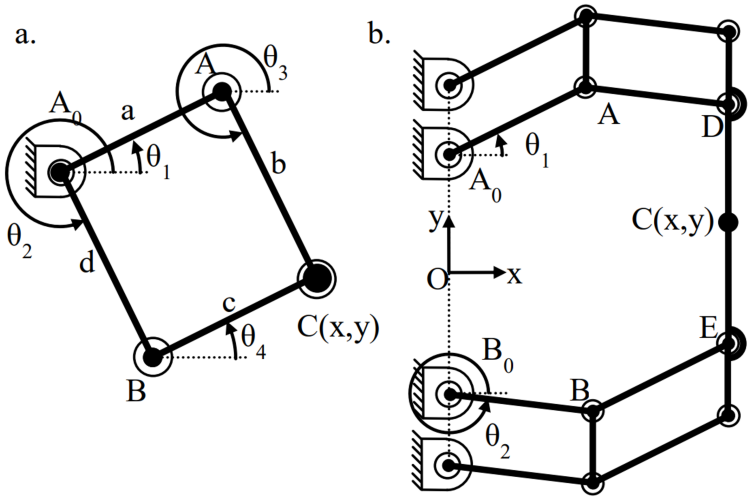

Figure 2.1. a) 5R Mechanism, b) 6R Over-constrained mechanism
(Source: Kiper et al. 2015)

The two mechanisms presented in Figure 2.1a and 2.1b are kinematically equivalent when the positioning of point C is of concern given that the corresponding link lengths are equal to each other, assuming that links and joints are rigid.

In the following, position level forward kinematics of hidden robot model is given:

$$\left|\overrightarrow{A_0A}\right| = \left|\overrightarrow{A_0B}\right| = \left|\overrightarrow{AC}\right| = \left|\overrightarrow{BC}\right| = l = 150\text{mm}$$

Because of the parallelogram loops; $\theta_1 = \theta_4,\ \theta_2 = \theta_3$

$$\vec{r_c} = \overrightarrow{A_0A} + \overrightarrow{AC} = \overrightarrow{A_0B} + \overrightarrow{BC} = l(e^{i\theta_1} + e^{i\theta_3}) = l(e^{i\theta_2} + e^{i\theta_4}) \tag{2.1}$$

$$\vec{r_c} = l(e^{i\theta_1} + e^{i\theta_2})$$

$$x = l[cos(\theta_1) + (cos(\theta_2)],\ y = l[sin(\theta_1) + (sin(\theta_2)]$$

Position level inverse kinematics:

$$\vec{r_c} = x + iy,\ |\vec{r_c}| = r,\ \phi = atan2(y, x)$$

$$\eta = \measuredangle A_0AC = acos(\frac{a^2 + r^2 - b^2}{2ar}) = acos(\frac{r}{2l})$$

$$\theta_1 = \phi + \eta,\ \theta_2 = \phi - \eta \tag{2.2}$$

$$\theta_3 = atan2(y - lsin\theta_1, x - lcos\theta_1)$$

$$\theta_4 = atan2(y - lsin\theta_2, x - lcos\theta_2)$$

Position level forward and inverse kinematics are given in Equation Sets 2.1 and 2.2. Detailed velocity and acceleration level kinematics can be found in (Özkahya, 2019).

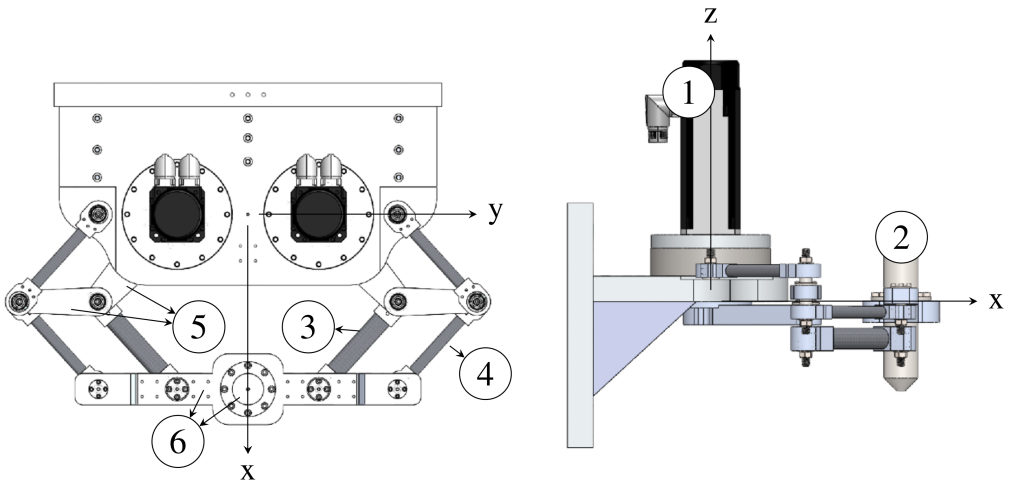

Figure 2.2. Top- and right-view of the 3D CAD model for the over-constrained mechanism; 1: motor and reducers, 2: Replica of the laser-head end-effector, 3: Thick distal links, 4: Thin links, 5: Aluminum links, 6: Platform including end-effector

In Figure 2.2, CAD model of the over-constrained mechanism is illustrated and some important components of the mechanism are explained.

2.3. Experimental Setup

In Figure 2.3, the experimental test setup to measure the compliant displacement of the end-effector is given. To measure the compliant displacement of the end-effector point of the mechanism Faro Prime Arm (±23 μm measurement accuracy) is used and to exert a force at any point in the workspace of the mechanism, a system that includes a 3D translational mechanism, calibrated weight and steel wire is used.

Faro Prime Arm is fixed to a 60 kg metal sheet by using a magnetic base ensures that the location of the Faro Prime Arm does not change while taking measurements. The center of gravity (CG) of the replica of the laser-head end-effector and the guide details are given in Figure 2.4. For clarity, the CG of the end-effector is defined with respect to the whole moving platform including end-effector (see Figure 2.2). Compliant displacement measurements at the CG can change with respect to mainly two factors. These factors are the a) measurement point on the mechanism, b) the force vector $\vec{F}$.

To acquire the compliant displacements at the CG of the platform as a 6-DoF information (3 translational displacements and 3 angular displacements), replica of the

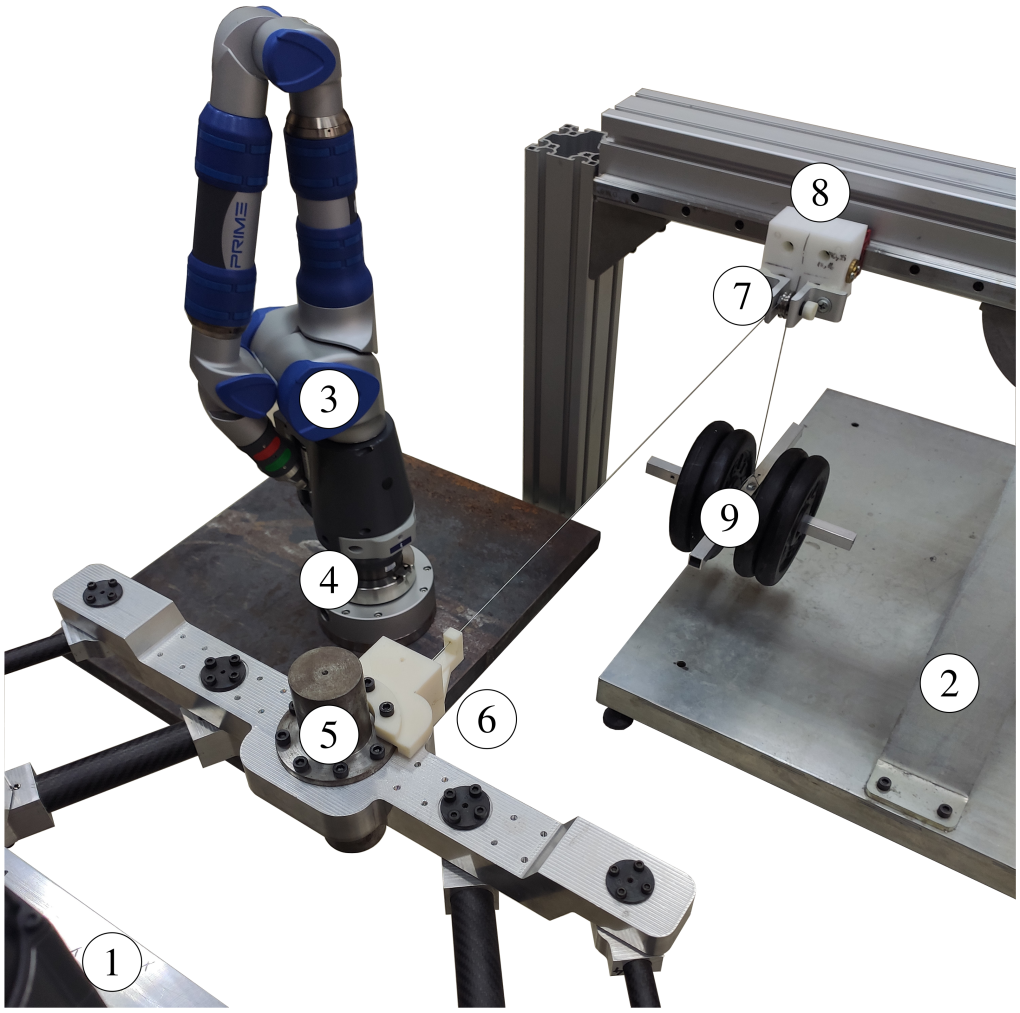

Figure 2.3. Experimental Test Setup; 1: 2-DoF planar mechanism, 2: Translational mechanism to arrange the force direction, 3: Faro Prime Arm, 4: Magnetic base, 5: Replica of laser head, 6: Guide, 7: Pulley, 8: Linear rail, 9: Calibrated weight

laser-head that contains 2 measurement points is designed and located at the end effector of the mechanism (Figure 2.4). By using $\overrightarrow{UL}$ information presented in Figure 2.4, compliant displacements at any point along the vertical-axis for the end effector of the mechanism can be derived. In this way, we can calculate the positional deviation of the laser beam on the workpiece. Since the distance between the laser head and the workpiece can change with respect to the material, laser power and the thickness of the workpiece, in this study, we used the CG point for our calculations. To obtain repeatable tests, calibrated masses are used to generate the magnitude of the exerted force at the end-effector. The direction of the external force is regulated by the use of a guide that is presented in Figure 2.4. The steel wire goes through the cylindrical hole ensures that the maximum

deviation of force direction is $1.37°$. That means, 99.97% of the loading will be in the desired direction if we neglect compliance of the mechanism because of the small forcing along other directions.

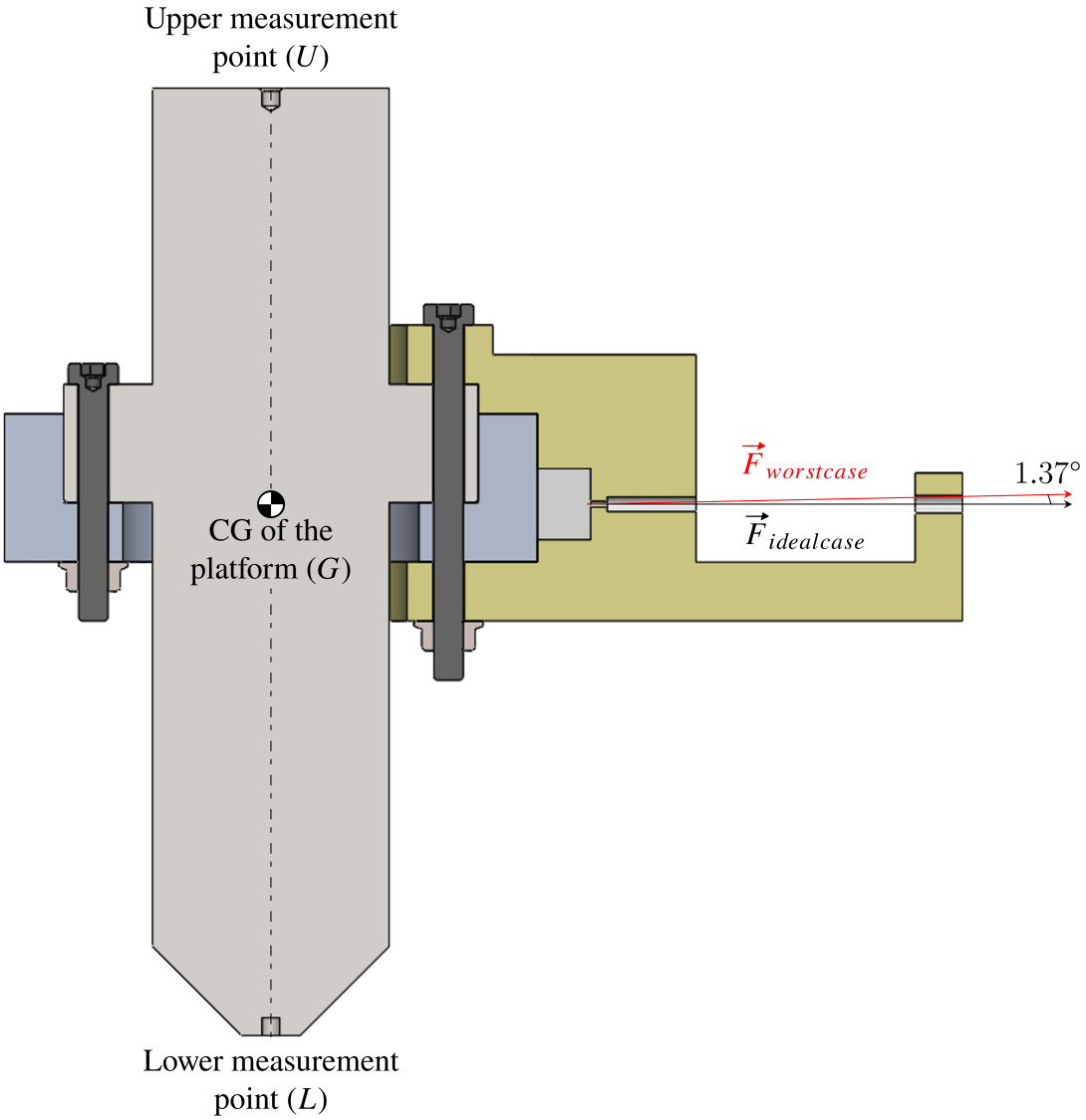

Figure 2.4. Replica of laser head and guide details: $|UG| = 69$ mm, $|UL| = 160$ mm

2.4. Experimental Procedure

The coordinate system of the robot is located between the two motors and the operational workspace of the robot is determined as 150 mm x 100 mm. In Figure 2.5, the coordinate system of the robot and 15 measurement points on the workspace are given.

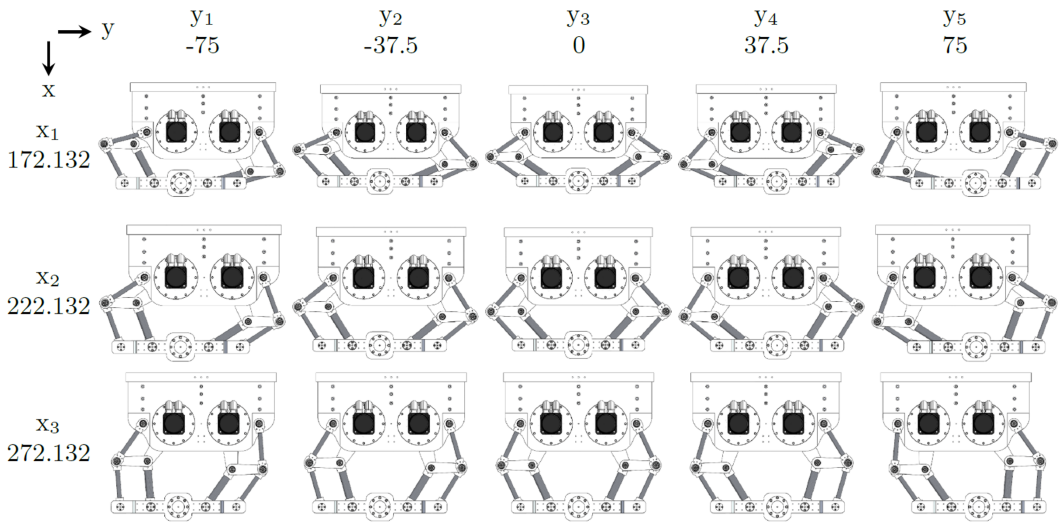

Figure 2.5. Mechanism configurations and end effector locations given in mm for the measurement points

At all measurement points of the workspace, the applied external forces are defined in steps in Table 2.1. In Step 0, there is a small amount of force because of the steel wire system. In each step, approximately 5 kg mass is added to system to exert a force and then, the coordinates of the upper measurement point (U) and Lower Measurement Point (L) are measured and recorded (Figure 2.4).

Table 2.1. Applied external force at the center of gravity of the end-effector of the mechanism to measure the compliances

Step	**Exerted Force (kgf)**	**$\approx$ in (N)**
0	0.11	0
1	5	50
2	9.92	100
3	14.89	150
4	19.83	200
5	24.86	250

To determine the location of CG of the platform (G) Equation Set 2.3, is used. If $\overrightarrow{UL}$ is known for each step, then both translational and angular compliant displacements of the platform can be found.

$$\vec{U} = U_x\,\vec{i} + U_y\,\vec{j} + U_z\,\vec{k}\,,\ \vec{L} = L_x\,\vec{i} + L_y\,\vec{j} + L_z\,\vec{k}$$
$$\overrightarrow{UL} = (L_x - U_x)\,\vec{i} + (L_y - U_y)\,\vec{j} + (L_z - U_z)\,\vec{k} \tag{2.3}$$
$$\vec{G} = \vec{U} + \frac{69}{160}\overrightarrow{UL}$$

2.5. Test Results

In Table 2.2, the translational compliant displacements under the forces (50-250 N) along $+x$-direction are given. As it was expected, because of the symmetrical structure of the mechanism, there are no Δy displacement for the points that are located on $+x$-axis ($y = 0$ mm) while the forces are increasing at $+x$-direction.

Table 2.2. OC - Compliant displacements of the CG of the end-effector under the forces along $+x$-direction (mm)

$\vec{F}$ in $\vec{x}$	Δx	Δy	Δz	Δx	Δy	Δz	Δx	Δy	Δz	Δx	Δy	Δz	Δx	Δy	Δz
	x_1y_1 (172.132,-75)			**x_1y_2 (172.132,-37.5)**			**x_1y_3 (172.132,0)**			**x_1y_4 (172.132,37.5)**			**x_1y_5 (172.132,75)**		
50N	0.105	0.061	-0.031	0.035	0.027	-0.009	0.027	0.002	-0.011	0.044	-0.024	-0.017	0.088	-0.058	-0.022
100N	0.198	0.109	-0.039	0.085	0.047	-0.016	0.059	0.002	-0.018	0.091	-0.040	-0.028	0.182	-0.094	-0.028
150N	0.289	0.164	-0.046	0.132	0.068	-0.030	0.094	0.000	-0.044	0.137	-0.059	-0.045	0.279	-0.151	-0.047
200N	0.389	0.205	-0.060	0.180	0.080	-0.051	0.129	-0.006	-0.056	0.184	-0.077	-0.057	0.369	-0.190	-0.055
250N	0.479	0.257	-0.080	0.226	0.096	-0.065	0.164	-0.009	-0.067	0.231	-0.099	-0.066	0.462	-0.232	-0.070
	x_2y_1 (222.132,-75)			**x_2y_2 (222.132,-37.5)**			**x_2y_3 (222.132,0)**			**x_2y_4 (222.132,37.5)**			**x_2y_5 (222.132,75)**		
50N	0.045	0.039	-0.020	0.027	0.019	0.008	0.024	-0.003	-0.023	0.027	-0.014	-0.012	0.044	-0.042	-0.015
100N	0.085	0.083	-0.031	0.054	0.036	-0.021	0.054	-0.005	-0.041	0.058	-0.026	-0.030	0.089	-0.084	-0.041
150N	0.131	0.118	-0.051	0.087	0.048	-0.026	0.083	-0.001	-0.059	0.091	-0.041	-0.031	0.133	-0.126	-0.054
200N	0.176	0.151	-0.073	0.120	0.062	-0.047	0.111	0.007	-0.068	0.118	-0.056	-0.048	0.178	-0.153	-0.064
250N	0.218	0.201	-0.081	0.147	0.077	-0.064	0.140	0.002	-0.079	0.147	-0.074	-0.070	0.220	-0.200	-0.091
	x_3y_1 (272.132,-75)			**x_3y_2 (272.132,-37.5)**			**x_3y_3 (272.132,0)**			**x_3y_4 (272.132,37.5)**			**x_3y_5 (272.132,75)**		
50N	0.039	0.088	-0.023	0.022	0.027	-0.023	0.012	0.002	-0.016	0.020	-0.029	-0.016	0.039	-0.085	-0.023
100N	0.084	0.181	-0.052	0.050	0.070	-0.035	0.031	0.001	-0.030	0.043	-0.064	-0.037	0.084	-0.175	-0.041
150N	0.124	0.275	-0.054	0.075	0.104	-0.070	0.048	0.000	-0.055	0.068	-0.101	-0.061	0.128	-0.270	-0.065
200N	0.170	0.359	-0.077	0.098	0.138	-0.087	0.071	-0.006	-0.079	0.094	-0.140	-0.080	0.167	-0.348	-0.082
250N	0.209	0.447	-0.104	0.117	0.175	-0.105	0.094	-0.003	-0.096	0.114	-0.164	-0.090	0.208	-0.430	-0.107

Also, absolute magnitudes of the translational displacement values are found to be symmetrical with respect to the $+x$-axis taking into account the resolution of the measurement system (±23 μm for Faro Prime Arm). These two observations are obtained from the measurement results to verify the test procedure's suitability. Moreover, while forces are increasing linearly along $+x$-direction 50 N to 250 N, the displacements are also increasing linearly. For instance, the displacement values for the measurement point (172.123, -75) are increasing linearly as the external force is increased linearly (0.1 mm

for 50 N, 0.2 mm for 100 N, etc.). These results suggest that for each point there is almost a linear relationship between the external force and compliant displacements along at the x- and y-directions.

Table 2.3. OC - Compliant displacements of the CG of the end-effector under the forces along $-y$-direction (mm)

$\vec{F}$ in $-\vec{y}$	Δx	Δy	Δz	Δx	Δy	Δz	Δx	Δy	Δz	Δx	Δy	Δz	Δx	Δy	Δz
	x_1y_1 (172.132,-75)			**x_1y_2 (172.132,-37.5)**			**x_1y_3 (172.132,0)**			**x_1y_4 (172.132,37.5)**			**x_1y_5 (172.132,75)**		
50N	-0.069	-0.079	-0.006	-0.026	-0.091	-0.001	-0.003	-0.084	0.006	0.022	-0.078	-0.003	0.054	-0.086	0.007
100N	-0.110	-0.190	-0.007	-0.047	-0.182	0.003	0.002	-0.172	0.008	0.051	-0.168	0.017	0.113	-0.182	0.016
150N	-0.177	-0.283	-0.012	-0.074	-0.268	0.002	-0.013	-0.246	0.006	0.071	-0.256	0.005	0.160	-0.273	0.012
200N	-0.243	-0.374	-0.019	-0.090	-0.357	0.001	-0.020	-0.326	0.010	0.088	-0.335	0.007	0.216	-0.359	0.013
250N	-0.309	-0.473	-0.033	-0.115	-0.449	0.001	-0.019	-0.420	0.005	0.117	-0.434	0.019	0.266	-0.449	0.015
	x_2y_1 (222.132,-75)			**x_2y_2 (222.132,-37.5)**			**x_2y_3 (222.132,0)**			**x_2y_4 (222.132,37.5)**			**x_2y_5 (222.132,75)**		
50N	-0.033	-0.133	-0.005	-0.031	-0.115	-0.009	-0.004	-0.110	0.004	0.020	-0.120	0.000	0.055	-0.122	0.011
100N	-0.078	-0.258	-0.009	-0.040	-0.243	-0.006	0.001	-0.232	0.006	0.050	-0.236	0.006	0.087	-0.251	0.013
150N	-0.114	-0.384	-0.015	-0.063	-0.366	-0.006	0.004	-0.357	0.013	0.065	-0.358	0.008	0.129	-0.375	0.021
200N	-0.161	-0.509	-0.008	-0.077	-0.488	-0.012	0.002	-0.475	0.014	0.083	-0.473	0.000	0.174	-0.499	0.014
250N	-0.204	-0.638	-0.016	-0.099	-0.609	-0.006	0.009	-0.604	0.009	0.099	-0.593	0.005	0.205	-0.628	0.014
	x_3y_1 (272.132,-75)			**x_3y_2 (272.132,-37.5)**			**x_3y_3 (272.132,0)**			**x_3y_4 (272.132,37.5)**			**x_3y_5 (272.132,75)**		
50N	-0.061	-0.346	-0.004	-0.039	-0.265	-0.009	-0.002	-0.246	0.000	0.038	-0.255	0.001	0.098	-0.319	0.000
100N	-0.148	-0.685	-0.009	-0.071	-0.532	-0.010	0.009	-0.494	-0.023	0.077	-0.523	-0.005	0.193	-0.658	-0.010
150N	-0.261	-1.001	-0.026	-0.105	-0.789	-0.014	0.013	-0.755	-0.014	0.118	-0.792	-0.002	0.275	-0.998	-0.005
200N	-0.335	-1.349	-0.023	-0.140	-1.052	-0.015	0.003	-0.990	-0.014	0.155	-1.042	0.004	0.358	-1.331	-0.012
250N	-0.421	-1.690	-0.028	-0.182	-1.319	-0.016	0.011	-1.251	-0.008	0.195	-1.305	0.002	0.458	-1.671	-0.009

In Table 2.3, the translational compliant displacements under the forces (50-250N) along $-y$-direction are given. This time, due to the symmetry there are no Δx displacement at the $+x$-axis while the external load is applied $-y$-direction. The symmetrical compliant displacement magnitudes with respect to the $+x$-axis are obtained and almost a linear relationship can be seen again.

2.6. Summary

As a result of this chapter, the compliance behavior of a 2-DoF planar over-constrained mechanism is gathered by using a test setup including Faro Prime arm as coordinate-measurement machine and a combination of 3D translational mechanism and steel-wire equipment as external force application system. This compliance information is used in Chapter 4 to improve the positioning accuracy of the 2-DoF planar over-constrained mechanism during high acceleration (up to 5 g) operation.

CHAPTER 3

STIFFNESS AND REPEATIBILITY COMPARISON

3.1. Introduction

Based on kinematic architecture, industrial robots can be classified into three groups as serial, parallel and hybrid robots. While serial robots have open-loop kinematic chains including a series of links connected to each other by motor actuated joints, parallel robots have closed-loop kinematic chains that contain more than one serial chain actuated by joint and hybrid robots are a mixture of them. Hybrid manipulators can show both serial and parallel manipulator properties depending on the application thereby comparison of serial and parallel robots is sufficient.

Merlet and Gosselin (2008) states that the links of the Gough platform (a parallel manipulator) show tension/compression characteristics while in working condition and undergoes no bending. Therefore, it leads to small deformations and good positioning accuracy. In addition, uncertainty in joint level decreases and therefore it causes good repeatability. Patel et al. (2012) have presented some beneficial features of parallel robots over serial robots. which are higher load capacity, low inertia, higher structural stiffness characteristics, and precise positioning. In parallel manipulators, containing more than one serial chain connected to the end-effector provides carrying a higher load with respect to the serial manipulators. Also, actuators mounted at the base lead to a robot with less moving mass and it results in a low inertia manipulator. In parallel robots, because of the parallel links and closed loops, joint errors are shared instead of accumulated, and in fact, that parallel robots are inherently more accurate than serial robots. In Table 3.1 a comparison between serial and parallel robots is given in terms of some noteworthy features. Before explaining the over-constrained 6R and simply-constrained 6R mechanism, it is better to explain the Grübler-Kutzbach mobility criterion given in Equation 3.1. This equation defines the number of degree-of-freedom (DoF) of the mechanism with respect to the parameters where λ is the DoF of the space ($\lambda = 3$ for planar and spherical space, $\lambda = 6$ for spatial space), L is the number of links, J is the number of joints and f_k is the DoF of the k^{th} joint.

Table 3.1. Comparison between serial and parallel robots in terms of some noteworthy features

Feature	Serial Robot	Parallel Robot
Forward Kinematic Computation	Easy	Difficult
Inverse Kinematic Computation	Difficult	Easy
Workspace	Large	Small
Position error	Accumulates	Averages
Stiffness characteristics	Low	High
Repeatibility	Low	High
Uncertainty in Joint Level	High	Low
Accuracy	Low	High

$$M = \lambda(L - J - 1) + \sum_{k=1}^{n} f_k \tag{3.1}$$

In the following, DoF of the 6R planar mechanism (M_{6R}), simply-constrained 6R mechanism (M_{SC}) and over-constrained 6R mechanism (M_{OC}), are calculated (Equation 3.2).

$$\begin{aligned} M_{6R} &= 3(6 - 6 - 1) + \sum_{k=1}^{6} 1 = 3 \\ M_{SC} &= 3(11 - 14 - 1) + \sum_{k=1}^{14} 1 = 2 \\ M_{OC} &= 3(12 - 16 - 1) + \sum_{k=1}^{16} 1 = 1 \end{aligned} \tag{3.2}$$

The 6R planar mechanism has 3-DoF as 2 translation motions and 1 angular motion in a plane. For the simply-constrained 6R mechanism is the angular motion in a plane is restricted and the end-effector can only translate x- and y-directions. When it comes to the over-constrained 6R mechanism, the DoF of the mechanism is seen as 1. However, in practice, it shows the same mobility characteristics with a simply-constrained 6R mechanism. If the mechanism provides more mobility than calculated this formula then, it is called over-constrained. In the Figure 3.1, the structural difference between the over-constrained and simply-constrained mechanism can be seen.

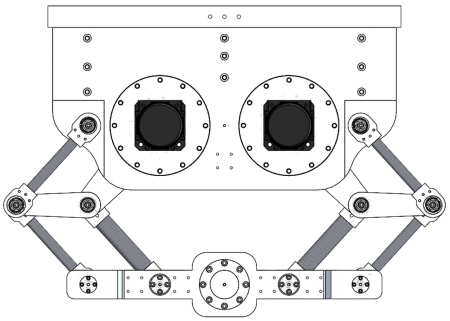

(a) Over-constrained 6R mechanism
(2-DoF Over-constrained mechanism)

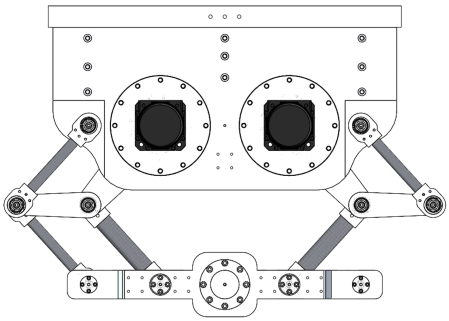

(b) Simply-constrained 6R mechanism
(2-DoF parallel mechanism)

Figure 3.1. Structural difference between over-constrained and parallel mechanism

3.2. Repeatability Comparison

In this section, repeatability of the mechanisms is compared at the static condition by measuring 9 different points 3 times. The configurations at the defined points can be seen in Figure 2.5. As a measurement device, Faro Prime Arm is used. These repeatability tests are conducted after the force balancing, frequency and compliance measurements tests are executed in order to observe how affected calibration of the mechanism.

Table 3.2. Repeatability and positioning accuracy performance of over-constrained mechanism (mm)

Trial	err_x	err_y	err_x	err_y	err_x	err_y
	$\mathbf{x_1y_1}$ **(172.132,-75)**		$\mathbf{x_1y_3}$ **(172.132,0)**		$\mathbf{x_1y_5}$ **(172.132,75)**	
1	0.794	0.312	0.473	0.017	0.249	0.851
2	0.791	0.31	0.471	0.018	0.246	0.851
3	0.792	0.31	0.474	0.018	0.246	0.853
Max Diff.	**0.003**	**0.002**	**0.003**	**0.001**	**0.003**	**0.002**
	$\mathbf{x_2y_1}$ **(222.132,-75)**		$\mathbf{x_2y_3}$ **(222.132,0)**		$\mathbf{x_2y_5}$ **(222.132,75)**	
1	0.556	0.139	0.347	0.042	0.058	0.246
2	0.558	0.142	0.345	0.043	0.054	0.25
3	0.557	0.14	0.344	0.045	0.059	0.242
Max Diff.	**0.002**	**0.003**	**0.003**	**0.003**	**0.005**	**0.008**
	$\mathbf{x_3y_1}$ **(272.132,-75)**		$\mathbf{x_3y_3}$ **(272.132,0)**		$\mathbf{x_3y_5}$ **(272.132,75)**	
1	0.504	0.122	0.265	0.103	0.06	0.033
2	0.504	0.124	0.263	0.106	0.063	0.028
3	0.506	0.125	0.263	0.106	0.061	0.025
Max Diff.	**0.002**	**0.003**	**0.002**	**0.003**	**0.003**	**0.008**

In Table 3.2, repeatability performance of the over-constrained mechanism can be seen. The terms err_x and err_y defines the positional errors along the x- and y-directions respectively. Because the accuracy of the CMM is about ±23 μm, it can be said that the maximum differences of the positioning errors in the over-constrained mechanism are below the measurement accuracy.

Table 3.3. Repeatability and positioning accuracy performance of simply-constrained mechanism (mm)

Trial	err_x	err_y	err_x	err_y	err_x	err_y
	x_1y_1 (172.132,-75)		**x_1y_3 (172.132,0)**		**x_1y_5 (172.132,75)**	
1	0.792	0.147	0.401	0.118	0.152	0.607
2	0.76	0.158	0.39	0.116	0.144	0.599
3	0.753	0.166	0.389	0.101	0.137	0.564
Max Diff.	**0.039**	**0.019**	**0.012**	**0.017**	**0.015**	**0.043**
	x_2y_1 (222.132,-75)		**x_2y_3 (222.132,0)**		**x_2y_5 (222.132,75)**	
1	0.348	0.213	0.169	0.276	0.009	0.304
2	0.342	0.205	0.169	0.25	0.008	0.284
3	0.347	0.197	0.17	0.244	0.004	0.265
Max Diff.	**0.006**	**0.016**	**0.001**	**0.032**	**0.005**	**0.039**
	x_3y_1 (272.132,-75)		**x_3y_3 (272.132,0)**		**x_3y_5 (272.132,75)**	
1	0.275	0.276	0.062	0.213	0.116	0.095
2	0.279	0.279	0.059	0.203	0.105	0.081
3	0.278	0.276	0.052	0.199	0.089	0.054
Max Diff.	**0.004**	**0.003**	**0.01**	**0.014**	**0.027**	**0.041**

In Table 3.3, repeatability performance for the simply-constrained mechanism is given. The magnitudes of the maximum differences are increased at all measurement points. The maximum difference between the positional errors are 0.039 mm for err_x at x_1y_1 and 0.043 mm for err_y at x_1y_5.

3.3. Stiffness Performance Comparison

In this section, stiffness characteristics of the over-constrained and parallel mechanism are compared in terms of angular and translational compliances by using the procedure given in Section 2.4. In Table 3.4, angular deflections of the over-constrained mechanism under the forces in x-direction is given. As it is expected, because of the symmetric configuration of the mechanism, there are small angular deflections about the x-axis in the accuracy range of the measurement device.

Table 3.4. Angular deflections of the OC mechanism under the forces along x-direction (degrees)

$\vec{F}$ in $\vec{x}$	Angular deflections about x-axis					Angular deflections about y-axis				
	x_1y_1	x_1y_2	x_1y_3	x_1y_4	x_1y_5	x_1y_1	x_1y_2	x_1y_3	x_1y_4	x_1y_5
50N	0.000	0.002	-0.001	-0.001	0.000	0.025	0.015	0.014	0.015	0.015
100N	-0.008	0.003	-0.002	0.005	0.008	0.036	0.032	0.028	0.033	0.031
150N	-0.006	0.004	-0.006	0.008	0.003	0.052	0.052	0.045	0.048	0.044
200N	-0.013	0.000	-0.004	0.008	0.012	0.064	0.065	0.062	0.064	0.061
250N	-0.019	-0.001	-0.003	0.009	0.016	0.077	0.082	0.078	0.077	0.073
	x_2y_1	x_2y_2	x_2y_3	x_2y_4	x_2y_5	x_2y_1	x_2y_2	x_2y_3	x_2y_4	x_2y_5
50N	0.000	0.003	-0.003	0.001	-0.006	0.016	0.016	0.017	0.017	0.017
100N	0.006	-0.002	-0.003	0.004	-0.003	0.036	0.029	0.034	0.032	0.034
150N	0.000	0.001	-0.006	0.005	-0.004	0.050	0.045	0.049	0.046	0.050
200N	-0.005	-0.001	0.000	0.007	0.004	0.066	0.062	0.067	0.062	0.067
250N	0.001	-0.004	0.001	0.004	0.002	0.084	0.076	0.082	0.079	0.082
	x_3y_1	x_3y_2	x_3y_3	x_3y_4	x_3y_5	x_3y_1	x_3y_2	x_3y_3	x_3y_4	x_3y_5
50N	0.002	0.001	0.003	0.004	-0.001	0.016	0.018	0.016	0.015	0.017
100N	0.000	0.001	0.002	0.005	0.001	0.036	0.035	0.031	0.034	0.031
150N	0.003	0.003	0.003	0.004	0.023	0.051	0.054	0.049	0.053	0.055
200N	0.004	-0.001	-0.002	0.005	0.000	0.069	0.070	0.068	0.070	0.069
250N	-0.004	0.003	0.002	0.011	-0.004	0.085	0.086	0.084	0.086	0.086

Table 3.5. Angular deflections of the OC mechanism under the forces along $-y$-direction (degrees)

$\vec{F}$ in $-\vec{y}$	Angular deflections about x-axis					Angular deflections about y-axis				
	x_1y_1	x_1y_2	x_1y_3	x_1y_4	x_1y_5	x_1y_1	x_1y_2	x_1y_3	x_1y_4	x_1y_5
50N	0.006	0.006	0.008	0.006	0.006	0.000	0.001	-0.001	0.000	-0.004
100N	0.016	0.015	0.012	0.018	0.016	0.010	0.007	0.000	0.000	0.001
150N	0.025	0.021	0.015	0.023	0.021	0.016	0.004	-0.010	-0.001	0.000
200N	0.029	0.031	0.017	0.030	0.029	0.014	0.009	-0.009	-0.006	-0.006
250N	0.034	0.036	0.021	0.040	0.038	0.019	0.009	-0.007	-0.001	-0.009
	x_2y_1	x_2y_2	x_2y_3	x_2y_4	x_2y_5	x_2y_1	x_2y_2	x_2y_3	x_2y_4	x_2y_5
50N	0.011	0.005	0.006	0.005	0.015	0.009	-0.007	-0.003	0.002	0.005
100N	0.017	0.015	0.017	0.017	0.015	0.011	-0.001	-0.003	0.006	0.008
150N	0.028	0.019	0.024	0.024	0.023	0.018	0.000	-0.002	0.003	0.002
200N	0.037	0.029	0.032	0.032	0.032	0.013	0.001	-0.005	0.007	0.006
250N	0.044	0.034	0.038	0.040	0.036	0.015	-0.002	0.000	0.003	0.003
	x_3y_1	x_3y_2	x_3y_3	x_3y_4	x_3y_5	x_3y_1	x_3y_2	x_3y_3	x_3y_4	x_3y_5
50N	0.015	0.004	0.007	0.009	0.015	0.010	0.000	-0.002	0.002	0.004
100N	0.023	0.013	0.018	0.017	0.019	0.016	0.003	0.005	0.007	0.006
150N	0.028	0.025	0.021	0.022	0.027	0.009	0.004	0.010	0.015	0.010
200N	0.045	0.035	0.029	0.040	0.035	0.017	0.006	0.004	0.006	0.011
250N	0.057	0.035	0.044	0.052	0.052	0.024	0.004	0.011	0.009	0.016

At measurement points x_1y_1 and x_1y_5, it can be seen there are increasing angular deflections at the opposite directions because the configuration of the mechanism is far away from the symmetric condition.

Table 3.6. Angular deflections of the SC mechanism under the forces along x-direction (degrees)

$\vec{F}$ in $\vec{x}$	Angular deflections about x-axis					Angular deflections about y-axis				
	x_1y_1	x_1y_2	x_1y_3	x_1y_4	x_1y_5	x_1y_1	x_1y_2	x_1y_3	x_1y_4	x_1y_5
50N	0.011	-0.003	-0.006	-0.003	0.013	0.045	0.026	0.018	0.009	-0.001
100N	0.014	-0.001	-0.001	0.000	0.024	0.077	0.061	0.039	0.020	-0.001
150N	0.019	-0.001	-0.003	0.005	0.034	0.115	0.087	0.060	0.029	-0.007
200N	0.028	0.001	-0.001	0.009	0.048	0.151	0.120	0.083	0.037	0.000
250N	0.027	0.007	0.003	0.010	0.056	0.195	0.159	0.106	0.049	-0.003
	x_2y_1	x_2y_2	x_2y_3	x_2y_4	x_2y_5	x_2y_1	x_2y_2	x_2y_3	x_2y_4	x_2y_5
50N	0.001	-0.001	0.003	-0.004	0.014	0.036	0.027	0.019	0.011	0.006
100N	0.004	0.001	0.004	0.003	0.015	0.071	0.057	0.041	0.020	0.013
150N	0.013	0.000	0.005	0.001	0.023	0.106	0.088	0.063	0.038	0.020
200N	0.013	0.000	0.004	0.001	0.024	0.144	0.117	0.083	0.050	0.022
250N	0.019	0.006	0.002	0.004	0.034	0.180	0.146	0.107	0.061	0.030
	x_3y_1	x_3y_2	x_3y_3	x_3y_4	x_3y_5	x_3y_1	x_3y_2	x_3y_3	x_3y_4	x_3y_5
50N	-0.005	0.010	-0.016	0.015	0.012	0.042	0.033	0.015	0.010	0.000
100N	0.001	0.008	-0.006	0.004	0.018	0.081	0.061	0.039	0.025	0.011
150N	-0.003	0.015	0.003	0.008	0.020	0.122	0.094	0.063	0.041	0.014
200N	0.006	0.020	-0.002	0.011	0.019	0.162	0.125	0.085	0.052	0.016
250N	0.009	0.013	0.010	0.007	0.015	0.204	0.154	0.110	0.068	0.019

For the angular deflections about the y-axis, one can say that all over the workspace of the mechanism there is an almost linear relationship between the exerted force and angular deflection. When it comes to the angular deflections because of the forces $-y$-direction given at Table 3.5, angular deflections about y-axis are smaller with respect to the angular deflections about x-axis. Also, it can be seen that the amount of the angular deflections because of the forces in $-y$-direction are smaller than that due to the forces x-direction. The smallest increase in the angular deflection about x-axis is observed for the measurement point x_1y_3 because, in that configuration, the higher amount of forces exerted at the axial direction of composite links.

In Table 3.6, angular deflections as a result of forces along the x-direction for the parallel mechanism are presented. Because the mechanism is not symmetric anymore, the angular deflections do not show regular distribution over the workspace and the amount of angular deflections is increased in both directions.

In Table 3.7, angular deflections because of the forces along the $-y$-direction for the parallel mechanism are given. The expected situation is while forces along $-y$-

direction, the angular deflection about the x-axis is higher. However, there was a strange fact while collecting compliance data for only this case. When the amount of calibrated weight increases, the linear rail always wants to slide along the $-x$-direction (See Figure 2.3). Probably, this situation and lower stiffness characteristics have caused higher angular deflections about y-axis.

Table 3.7. Angular deflections of the SC mechanism under the forces along $-y$-direction (degrees)

$\vec{F}$ in $-\vec{y}$	Angular deflections about x-axis					Angular deflections about y-axis				
	x_1y_1	x_1y_2	x_1y_3	x_1y_4	x_1y_5	x_1y_1	x_1y_2	x_1y_3	x_1y_4	x_1y_5
50N	-0.004	0.006	0.014	0.007	0.016	-0.008	-0.014	-0.014	-0.017	-0.020
100N	0.006	0.003	0.015	0.020	0.028	-0.015	-0.033	-0.035	-0.038	-0.035
150N	0.010	0.012	0.024	0.022	0.041	-0.022	-0.044	-0.053	-0.061	-0.056
200N	0.011	0.017	0.029	0.038	0.061	-0.034	-0.056	-0.073	-0.080	-0.073
250N	0.014	0.019	0.027	0.044	0.068	-0.039	-0.071	-0.095	-0.097	-0.093
	x_2y_1	x_2y_2	x_2y_3	x_2y_4	x_2y_5	x_2y_1	x_2y_2	x_2y_3	x_2y_4	x_2y_5
50N	0.006	0.008	0.011	0.013	0.017	-0.017	-0.030	-0.029	-0.027	-0.034
100N	0.010	0.010	0.017	0.019	0.028	-0.039	-0.059	-0.057	-0.058	-0.065
150N	0.008	0.017	0.025	0.033	0.042	-0.064	-0.079	-0.084	-0.085	-0.094
200N	0.013	0.009	0.035	0.042	0.056	-0.091	-0.119	-0.113	-0.111	-0.124
250N	0.014	0.024	0.041	0.056	0.071	-0.112	-0.133	-0.141	-0.147	-0.154
	x_3y_1	x_3y_2	x_3y_3	x_3y_4	x_3y_5	x_3y_1	x_3y_2	x_3y_3	x_3y_4	x_3y_5
50N	0.002	0.007	0.009	0.017	0.026	-0.061	-0.055	-0.052	-0.057	-0.064
100N	0.002	0.015	0.018	0.035	0.043	-0.121	-0.114	-0.104	-0.112	-0.130
150N	0.004	0.016	0.026	0.043	0.062	-0.177	-0.171	-0.162	-0.171	-0.195
200N	0.010	0.027	0.034	0.053	0.072	-0.242	-0.222	-0.217	-0.237	-0.270
250N	0.010	0.030	0.054	0.066	0.099	-0.305	-0.283	-0.274	-0.294	-0.342

In the following, translational compliant displacements of the CG are given for the parallel mechanism (simply-constrained mechanism). The translational compliant displacements for the over-constrained mechanism are presented in Section 2.5. In Tables 3.8 and 3.9, translational compliant displacements as a result of forces along the x- and $-y$-directions are given respectively. It can be seen that if we compare the maximum translational compliant displacements of two mechanisms, the parallel mechanism has more than two times higher translational compliant displacements for the forces both along x- and $-y$-directions. For example, at the measurement point x_1y_1, the total absolute compliant displacement for the over-constrained mechanism is 0.55mm under the forces in x-direction while this compliant displacement for the parallel mechanism is 1.53mm. For the forces along $-y$-direction at the measurement point x_3y_5, these compliant displacement values are 1.73 mm to 3.33 mm.

Table 3.8. SC - Compliant displacements of the CG of the end-effector under the forces along $+x$-direction (mm)

$\vec{F}$ in $\vec{x}$	Δx	Δy	Δz	Δx	Δy	Δz	Δx	Δy	Δz	Δx	Δy	Δz	Δx	Δy	Δz
	x_1y_1 (172.132,-75)			x_1y_2 (172.132,-37.5)			x_1y_3 (172.132,0)			x_1y_4 (172.132,37.5)			x_1y_5 (172.132,75)		
50N	0.215	0.102	-0.052	0.068	0.061	-0.021	0.030	0.007	-0.003	0.047	-0.037	0.000	0.153	-0.104	0.018
100N	0.424	0.218	-0.073	0.148	0.111	-0.054	0.069	0.017	-0.026	0.100	-0.074	-0.014	0.303	-0.195	0.001
150N	0.642	0.327	-0.103	0.231	0.165	-0.069	0.109	0.026	-0.048	0.153	-0.089	-0.029	0.450	-0.276	0.000
200N	0.870	0.454	-0.125	0.311	0.216	-0.097	0.147	0.041	-0.069	0.196	-0.128	-0.022	0.581	-0.377	0.000
250N	1.084	0.564	-0.188	0.410	0.293	-0.145	0.184	0.045	-0.098	0.245	-0.156	-0.037	0.700	-0.451	0.014
	x_2y_1 (222.132,-75)			x_2y_2 (222.132,-37.5)			x_2y_3 (222.132,0)			x_2y_4 (222.132,37.5)			x_2y_5 (222.132,75)		
50N	0.079	0.085	-0.034	0.038	0.049	-0.021	0.028	0.011	-0.013	0.028	-0.033	-0.013	0.062	-0.097	-0.006
100N	0.162	0.170	-0.068	0.083	0.098	-0.045	0.058	0.014	-0.027	0.057	-0.052	-0.016	0.113	-0.153	-0.012
150N	0.244	0.258	-0.094	0.132	0.144	-0.091	0.086	0.017	-0.062	0.094	-0.073	-0.037	0.169	-0.206	-0.017
200N	0.330	0.340	-0.141	0.181	0.186	-0.122	0.118	0.010	-0.082	0.126	-0.090	-0.051	0.212	-0.278	-0.023
250N	0.412	0.422	-0.167	0.225	0.235	-0.154	0.153	0.006	-0.107	0.151	-0.122	-0.061	0.266	-0.338	-0.026
	x_3y_1 (272.132,-75)			x_3y_2 (272.132,-37.5)			x_3y_3 (272.132,0)			x_3y_4 (272.132,37.5)			x_3y_5 (272.132,75)		
50N	0.083	0.182	-0.061	0.039	0.091	-0.046	0.014	0.021	0.012	0.019	-0.053	-0.003	0.050	-0.160	0.002
100N	0.171	0.384	-0.118	0.077	0.179	-0.080	0.036	0.043	-0.014	0.046	-0.115	-0.026	0.117	-0.318	0.000
150N	0.254	0.568	-0.176	0.115	0.287	-0.107	0.057	0.071	-0.038	0.072	-0.148	-0.048	0.166	-0.449	-0.008
200N	0.339	0.760	-0.200	0.153	0.362	-0.146	0.079	0.092	-0.067	0.095	-0.198	-0.057	0.211	-0.603	-0.013
250N	0.424	0.956	-0.274	0.190	0.433	-0.170	0.098	0.117	-0.097	0.123	-0.240	-0.086	0.264	-0.729	-0.014

Table 3.9. SC - Compliant displacements of the CG of the end-effector under the forces along $-y$-direction (mm)

$\vec{F}$ in $-\vec{y}$	Δx	Δy	Δz	Δx	Δy	Δz	Δx	Δy	Δz	Δx	Δy	Δz	Δx	Δy	Δz
	x_1y_1 (172.132,-75)			x_1y_2 (172.132,-37.5)			x_1y_3 (172.132,0)			x_1y_4 (172.132,37.5)			x_1y_5 (172.132,75)		
50N	-0.135	-0.125	-0.008	-0.057	-0.110	-0.004	-0.014	-0.107	0.011	0.037	-0.122	0.008	0.123	-0.130	0.009
100N	-0.242	-0.237	0.006	-0.122	-0.224	0.004	-0.032	-0.223	0.024	0.069	-0.242	0.026	0.226	-0.276	0.032
150N	-0.355	-0.359	0.018	-0.173	-0.339	0.016	-0.044	-0.339	0.037	0.095	-0.363	0.038	0.328	-0.408	0.057
200N	-0.476	-0.475	0.022	-0.223	-0.454	0.030	-0.062	-0.450	0.049	0.129	-0.489	0.061	0.432	-0.537	0.079
250N	-0.591	-0.595	0.028	-0.281	-0.570	0.035	-0.086	-0.560	0.056	0.160	-0.620	0.070	0.534	-0.688	0.094
	x_2y_1 (222.132,-75)			x_2y_2 (222.132,-37.5)			x_2y_3 (222.132,0)			x_2y_4 (222.132,37.5)			x_2y_5 (222.132,75)		
50N	-0.090	-0.188	0.019	-0.063	-0.180	0.024	-0.017	-0.166	0.031	0.031	-0.189	0.018	0.086	-0.212	0.023
100N	-0.179	-0.368	0.045	-0.119	-0.354	0.046	-0.028	-0.344	0.060	0.041	-0.375	0.044	0.145	-0.408	0.052
150N	-0.273	-0.556	0.078	-0.164	-0.536	0.078	-0.037	-0.526	0.084	0.077	-0.559	0.080	0.216	-0.614	0.096
200N	-0.370	-0.735	0.102	-0.233	-0.693	0.092	-0.046	-0.714	0.123	0.097	-0.752	0.112	0.282	-0.817	0.123
250N	-0.461	-0.922	0.120	-0.266	-0.887	0.124	-0.065	-0.896	0.149	0.118	-0.949	0.150	0.345	-1.014	0.161
	x_3y_1 (272.132,-75)			x_3y_2 (272.132,-37.5)			x_3y_3 (272.132,0)			x_3y_4 (272.132,37.5)			x_3y_5 (272.132,75)		
50N	-0.210	-0.616	0.071	-0.097	-0.474	0.072	-0.021	-0.440	0.068	0.049	-0.479	0.070	0.168	-0.628	0.088
100N	-0.413	-1.208	0.146	-0.197	-0.933	0.148	-0.044	-0.879	0.126	0.091	-0.948	0.143	0.303	-1.247	0.169
150N	-0.610	-1.806	0.240	-0.293	-1.410	0.207	-0.072	-1.325	0.208	0.132	-1.431	0.216	0.449	-1.868	0.260
200N	-0.820	-2.395	0.319	-0.391	-1.876	0.275	-0.103	-1.766	0.279	0.161	-1.922	0.297	0.602	-2.551	0.357
250N	-1.039	-3.009	0.405	-0.505	-2.407	0.355	-0.129	-2.212	0.352	0.202	-2.415	0.370	0.745	-3.215	0.452

3.4. Summary

This chapter illustrated the repeatability and compliance behavior of the over-constrained mechanism and parallel mechanism. As a summary, it proves that the over-constrained mechanism shows better repeatability characteristics and lower compliance values with respect to the parallel mechanism. Therefore, it solidifies the idea of using the over-constrained mechanism will give better results for a study that involves the enhancement of trajectory tracking accuracy by using the compliance model of the mechanism.

CHAPTER 4

ENHANCING TRAJECTORY TRACKING ACCURACY

4.1. Introduction

The mechanisms defined in Figure 3.1 are candidate micro-manipulators to be used in macro-micro manipulation for laser cutting processing. In industrial robotics, macro-micro manipulation can be defined as a robot with a gripper: the robot itself is the macro-manipulator and the gripper is being the micro-manipulator. In this case, defined micro-manipulators can be thought of as a gripper that actuates the higher accelerations up to 5 g and the macro-manipulator is a planar cartesian manipulator that is designed to have a relatively larger workspace (3 m by 1.5 m) that will actuate the lower accelerations up to 1 g. Limiting the acceleration of the macro-manipulation aims to prevent vibrational behavior due to the movement of the relatively higher mass and inertia. The general goal of the macro-micro manipulation laser cutting system is to shorten the task completion duration without sacrificing the trajectory tracking accuracy (Dede et al., 2016). However, in dynamic performances of the mechanisms (micro-manipulators), vibrational behavior is observed at the tip point of the end-effector while the acceleration is increasing.

In robotic-based machining, a robot is exposed to external forces as a result of interaction between the workpiece and the end-effector tool. Because of these external forces, deflections or compliances occur on the mechanism's elements that decrease the manufacturing accuracy. A new technique that estimates the compliances of the end-effector by using a non-linear stiffness model and reduced elastodynamic model of the robot. This estimation is done by creating an error function that predicts the compliances of the robot with respect to its configuration. For the milling process that is executed by the KUKA KR270 serial robot, the proposed procedure and algorithm are used to compensate the end-effector deflections (Klimchik et al., 2014).

In soft robotics, the elements of the soft robot like cables and elastic materials show compliant behavior while actuating it. Due to these elements generally including imperfections and uncertainties, it is better to use data-driven techniques to model the soft robot's quasi-static behavior. In the paper of Bern et al. (2020), the inverse kinematics

of the soft robot is modeled by using a neural network. The neural network inputs are chosen as actuators' inputs, and the end-effector position of the soft robot is chosen as the output of this neural network. The end-effector position is captured by a camera and recorded with corresponding control inputs to train the neural network. As a result, some trajectory following experiments are conducted in real-time and the performance of trajectory tracking of the soft robot is evaluated.

Benefits of over-constrained mechanism in the static condition are demonstrated in Section 3.1. However, the dynamic performances of these mechanisms are not compared yet. In the following sections of this chapter, assumptions and methodology are given to solve this vibrational behavior at the trajectory tracking. Then, dynamic performances of these two mechanisms for different configurations are evaluated using an image processing algorithm.

4.2. Compliance Model with Its Assumptions and Novelty

In theory, position level forward kinematics ($\bar{\kappa}_{FW}$) of the mechanism gives the end-effector position ($\bar{\kappa}_{EE}$). However, in a real case, the position of the end-effector depends on some parameters in addition to the forward kinematics. The detailed explanation that affects the accuracy of the end-effector position is given in Section 2.1. In this chapter, these parameters are reduced into 3 parameters which are positional change because of the gravity ($\bar{\kappa}_G$), positional change due to the internal stresses ($\bar{\kappa}_I$) and joint clearances ($\bar{\kappa}_J$) by eliminating the parameters that have a small effect on the end-effector accuracy. The first pose of the end-effector ($\bar{\kappa}_{EE}$) before the loading can be expressed with Equation 4.1.

$$\bar{\kappa}_{EE}^{(1)} = \bar{\kappa}_{FW}^{(1)} + \bar{\kappa}_{G}^{(1)} + \bar{\kappa}_{I}^{(1)} + \bar{\kappa}_{J}^{(1)} \tag{4.1}$$

In Equation 4.2, the second pose of the end-effector after the loading is given. The term $\boldsymbol{C}$ represents the compliance matrix of the mechanism and, $\bar{F}$ represents inertial forces and torques on the mechanism.

$$\bar{\kappa}_{EE}^{(2)} = \bar{\kappa}_{FW}^{(2)} + \bar{\kappa}_{G}^{(2)} + \bar{\kappa}_{I}^{(2)} + \bar{\kappa}_{J}^{(2)} + \hat{\boldsymbol{C}}\bar{F} \tag{4.2}$$

Over-constrained kinematic structure inherently leads to a different amount of internal stresses with respect to the mechanism configuration but besides that, it reduces the joint clearances to uncertainty level. Gravity affects the end-effector pose by exert-

ing various moments at the different locations of the end-effector. The effect of the joint clearances can be neglected because of the nature of the over-constrained mechanism and kinematic calibration can estimate not only the effects of internal stresses and gravity but also manufacturing and assembly errors. After the assumptions, the displacement matrix $\Delta\bar{\kappa}_{EE}$ can be explained as given in Equation 4.3.

$$\Delta\bar{\kappa}_{EE} = \bar{\kappa}_{EE}^{(2)} - \bar{\kappa}_{EE}^{(1)} = \hat{\boldsymbol{C}}\bar{F} \tag{4.3}$$

As another assumptions, the masses and moment of inertias of the links are neglected and only the mass of the end-effector (3.6 kg) is considered because the masses of the links are small with respect to the end-effector mass. As a result of this assumption Equation 4.3 is updated as in Equation 4.4. $\bar{F}_{EE}$ states that forcing on the point mass located at the center of gravity of end-effector including platform mass.

$$\Delta\bar{\kappa}_{EE} = \hat{\boldsymbol{C}}\bar{F}_{EE} \tag{4.4}$$

As a novelty of this study, it is proposed to correct the trajectory by considering the compliance displacements as a result of D'Alembert forces and it is suggested to perform this trajectory correction process by using the compliance information obtained from the stiffness tests performed in the static condition.

As further assumptions, the equations written above are derived for a 6-DoF forcing and pose. In this case, there is a 2-DoF planar over-constrained mechanism that operates at a plane. Therefore, the relevant parameters to be updated are x and y task space coordinates in order to increase the trajectory following accuracy of the mechanism, and one can say that there are two D'Alembert forces along the x- and y-directions that causes compliant displacements Δx and Δy. For clarity, defined end-effector displacement and forcing on the mechanism can be seen in Figure 4.5

$$\Delta\bar{\kappa}_{EE} = \begin{bmatrix} \Delta x \\ \Delta y \end{bmatrix} \quad \bar{F}_{EE} = \begin{bmatrix} F_x \\ F_y \end{bmatrix} \tag{4.5}$$

Compliance matrix depends on the parameters like mechanism configuration, mechanical properties of elements that are used in mechanism and dimensions of these elements. This compliance information is gathered experimentally at some measurement points as explained in Chapter 2 and detailed in Chapter 3. As a result of these measurements, it can be seen that the different amount of forcing F_x and/or F_y at a point defined in terms of task space coordinates (x, y) affects both Δx and Δy.

$$\begin{aligned}\Delta x &= \Delta x_{F_x} + \Delta x_{F_y} = f(x, y, F_x) + f(x, y, F_y) \\ \Delta y &= \Delta y_{F_x} + \Delta y_{F_y} = g(x, y, F_x) + g(x, y, F_y)\end{aligned} \tag{4.6}$$

To understand clearly Equation 4.6, as an example, Δx_{F_x} is the compliant displacement of end-effector along x-direction because of the F_x and $f(x, y, F_x)$ specifies that Δx_{F_x} is a function of parameters x, y and F_x.

At a specified measurement point (x, y), the compliant end-effector displacements is a function of only F_X and F_Y and it is given in Equation 4.7.

$$\begin{aligned}\Delta x_{ij} &= \Delta x_{ijF_x} + \Delta x_{ijF_y} = f(F_x) + f(F_y) \\ \Delta y_{ij} &= \Delta y_{ijF_x} + \Delta y_{ijF_y} = g(F_x) + g(F_y)\end{aligned} \tag{4.7}$$

The term ij indicates the end-effector location for measurement points as shown in Figure 2.5. For instance, Δx_{11} specifies the total compliant displacement at the x-direction of the top-left mechanism configuration in this figure and Δx_{11F_x} is the compliant displacement along the x-direction because of the forcing F_x at that measurement point. There is an almost linear relationship between the forcing and compliance at specified measurement points ss stated in Section 2.5. However, because of the internal stresses when there is no forcing on the mechanism, compliant displacements can occur. Then, there are 4 first-order polynomial functions for a measurement point in order to find compliant displacements Δx_{ij} and Δy_{ij}.

$$\begin{aligned}\Delta x_{ijF_x} &= m_{ij}F_x + n_{ij} \\ \Delta x_{ijF_y} &= o_{ij}F_y + p_{ij} \\ \Delta y_{ijF_y} &= s_{ij}F_x + u_{ij} \\ \Delta y_{ijF_y} &= v_{ij}F_y + w_{ij}\end{aligned} \tag{4.8}$$

Forces F_x and F_y are $F \approx [50\ 100\ 150\ 200\ 250]^T$ N as given in Table 2.1 and compliant displacements as a result of these external forces are given in Table 2.2 and 2.3. At each measurement point, there is a loading and measurement procedure that accomplished by 5 steps. In order to specify the step, a new parameter k is defined. After this information, Equation 4.8 can be rewritten in the matrix form.

$$\begin{bmatrix}\Delta x_{ijF_{kx}} & \Delta x_{ijF_{ky}} & \Delta y_{ijF_{kx}} & \Delta y_{ijF_{ky}}\end{bmatrix} = \begin{bmatrix}F_k & 1\end{bmatrix} \begin{bmatrix}m_{ij} & o_{ij} & s_{ij} & v_{ij} \\ n_{ij} & p_{ij} & u_{ij} & w_{ij}\end{bmatrix} \tag{4.9}$$

Open form of Equation 4.9 for $k = 1:5$ is given in Equation 4.10.

$$\underbrace{\begin{bmatrix} \Delta x_{ijF_{1x}} & \Delta x_{ijF_{1y}} & \Delta y_{ijF_{1x}} & \Delta y_{ijF_{1y}} \\ \Delta x_{ijF_{2x}} & \Delta x_{ijF_{2y}} & \Delta y_{ijF_{2x}} & \Delta y_{ijF_{2y}} \\ \Delta x_{ijF_{3x}} & \Delta x_{ijF_{3y}} & \Delta y_{ijF_{3x}} & \Delta y_{ijF_{3y}} \\ \Delta x_{ijF_{4x}} & \Delta x_{ijF_{4y}} & \Delta y_{ijF_{4x}} & \Delta y_{ijF_{4y}} \\ \Delta x_{ijF_{5x}} & \Delta x_{ijF_{5y}} & \Delta y_{ijF_{5x}} & \Delta y_{ijF_{5y}} \end{bmatrix}}_{\hat{B}} = \underbrace{\begin{bmatrix} F_1 & 1 \\ F_2 & 1 \\ F_3 & 1 \\ F_4 & 1 \\ F_5 & 1 \end{bmatrix}}_{\hat{A}} \underbrace{\begin{bmatrix} m_{ij} & o_{ij} & s_{ij} & v_{ij} \\ n_{ij} & p_{ij} & u_{ij} & w_{ij} \end{bmatrix}}_{\hat{Q}} \tag{4.10}$$

Then, the coefficients of first-order polynomial functions for any measurement point can be found by using the normal equation method of least squares as shown in Equation 4.11.

$$\hat{Q} = (\hat{A}^T \hat{A})^{-1} \hat{A}^T \hat{B} \tag{4.11}$$

After finding the coefficients of first order polynomial functions, Δx_{ij} and Δy_{ij} can be predicted by using Equations 4.8 and 4.7 respectively for any F_x and F_y forcing at that measurement point.

In order to find the compliant displacement values Δx and Δy for F_x and F_y forcing at any end-effector location (x, y) specified in the workspace of the mechanism, bilinear interpolation between the predicted compliant displacements of 15 measurement points is used (See Figure 4.1).

In the following Equation Set 4.12, an example bilinear interpolation formulation is given for the calculation of compliant displacements at point P.

$$\begin{aligned} \Delta x &= \frac{1}{(x_2 - x_1)(y_2 - y_1)} \begin{bmatrix} x_2 - x & x - x_1 \end{bmatrix} \begin{bmatrix} \Delta x_{11} & \Delta x_{12} \\ \Delta x_{21} & \Delta x_{22} \end{bmatrix} \begin{bmatrix} y_2 - y \\ y - y_1 \end{bmatrix} \\ \Delta y &= \frac{1}{(x_2 - x_1)(y_2 - y_1)} \begin{bmatrix} x_2 - x & x - x_1 \end{bmatrix} \begin{bmatrix} \Delta y_{11} & \Delta y_{12} \\ \Delta y_{21} & \Delta y_{22} \end{bmatrix} \begin{bmatrix} y_2 - y \\ y - y_1 \end{bmatrix} \end{aligned} \tag{4.12}$$

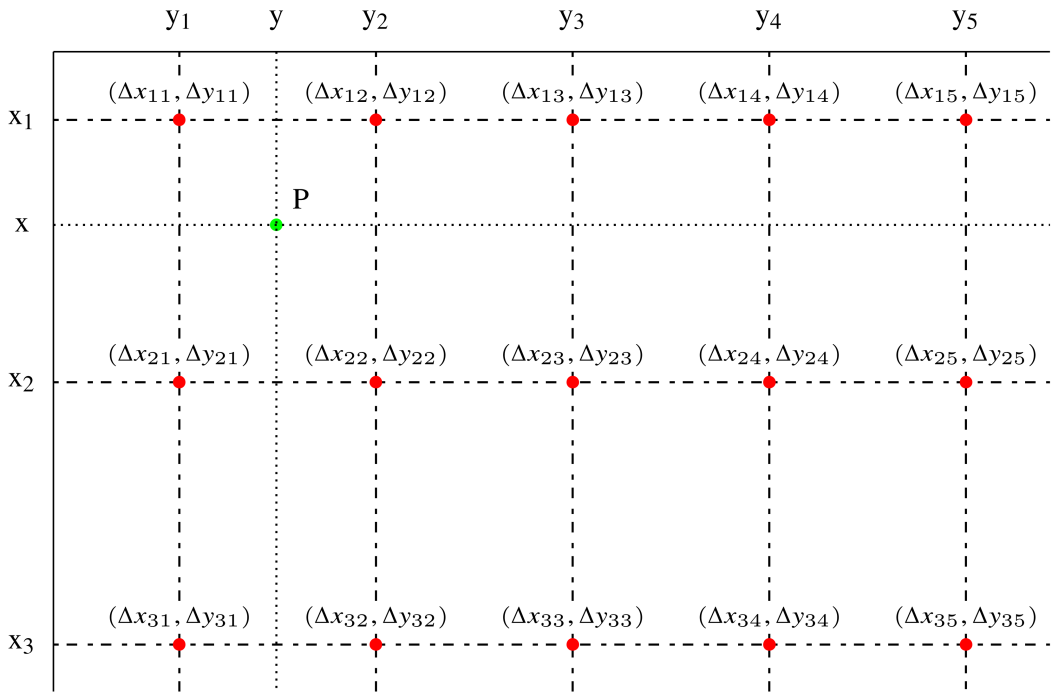

Figure 4.1. Bilinear interpolation between the predicted compliant displacements $(\Delta x_{ij}, \Delta y_{ij})$ of measurement points

4.3. Laser Marking System and Control Algorithm Details

Up to this point, assumptions made for modeling the compliant displacements of the mechanism are given, and also methods that are used for this modeling process are explained as least-squares normal equation and bilinear interpolation.

In Figure 4.2, the entire hardware setup of the mechanism can be seen. By using the CAM program, defined trajectories are converted to G-codes, and these G codes are transferred to the MATLAB software. According to the trajectory planning algorithm and kinematic equations, these G-codes converted to the motion demands for actuators. Then, joint level actuator inputs are fed to the servo drivers that include the PID controller. As a result of that control, the signal is transmitted to the actuators.

In Figure 4.3, the flow chart diagram for updating trajectory can be seen. Desired end-effector trajectory is found by using a trapezoidal acceleration profile in the motion planning step by limiting velocity, acceleration and jerk profiles. By taking the numerical derivative of discrete-time desired trajectory two times, end-effector accelerations can be found. The final assumption is while calculating the D'Alembert forces, rigid body kinematics are used. In practice, these end-effector accelerations will be different because of the compliance of the mechanism.

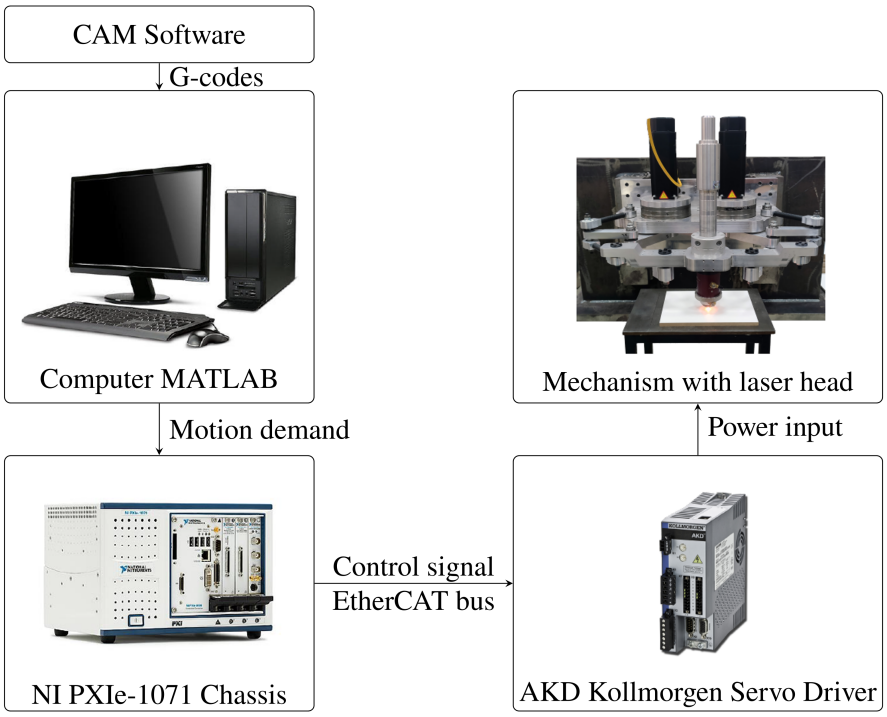

Figure 4.2. Hardware Setup

After estimating the D'Alembert forces, these forces and end-effector position are fed to the data-driven compliance model of the mechanism. As a result of that end-effector compliances are predicted and the trajectory is updated. The updated trajectory is given as input the inverse kinematics of the mechanism and then, output joint variables are transmitted to the actuators.

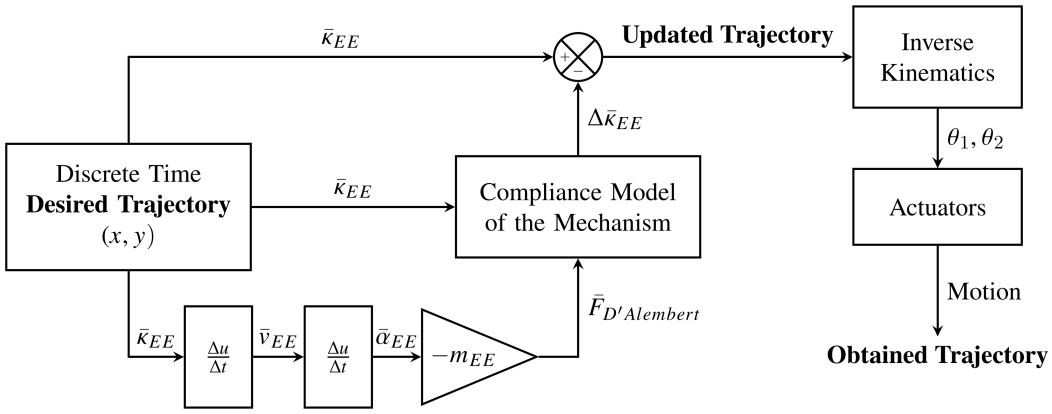

Figure 4.3. Flowchart Diagram for Updating Trajectory at 2kHz Sampling Rate

4.4. Importance of the End-effector's Center of Gravity Location

When a force is applied to a body it will produce a tendency for the body to rotate about a point that is not on the line of action of the force. In Figure 4.4, there is an L shape body that is fixed at the point O.

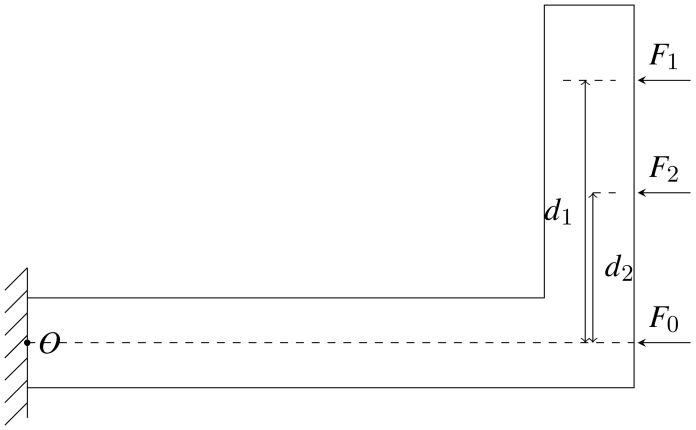

Figure 4.4. Moment of a force

There are two exerted forces F_1 and F_2 that have the same magnitude. Due to the different vertical distances to the fixed point O, these forces will create a different amount of moments that will result in different amounts of bending. If the line of action of the exerted force passes through the fixed point O, there will be no moment on the body. This is the case for the exerted force F_0 and the body will be exposed to deformation only along the axial direction. If we look at the mechanism from the right view as seen in the 2.2b, the mechanism can be thought of as a simple L shape. Because the laser head's mass accounts for roughly half of the platform's mass, the location of the laser head is important for arranging the CG position of the platform, which also determines the location of the D'Alembert forces under dynamic conditions. In Figure 4.5, there are two different assemblies of laser head can be seen. In Figure 4.5a, the over-constrained mechanism with the upper laser head position G_U can be seen and in In Figure 4.5b, the mechanism with the lower laser head position G_L can be seen. The dimensions $\left|\overrightarrow{G_U G}\right|$ and $\left|\overrightarrow{G_L G}\right|$ can be thought as d_1 and d_2 respectively.

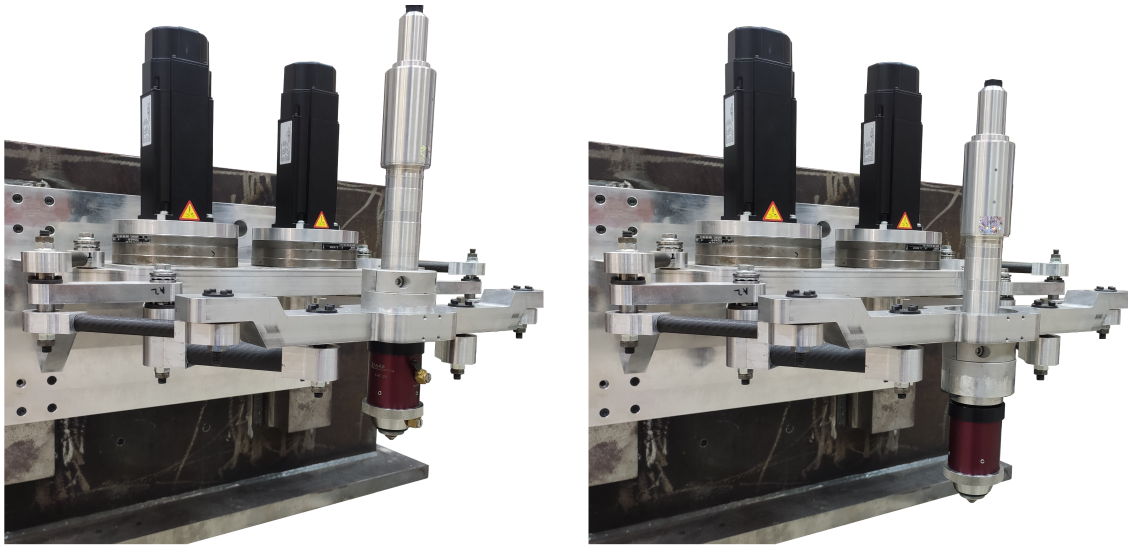

(a) Upper laser head position G_U
$\left|\overrightarrow{G_U G}\right| = 35.9\text{mm}$

(b) Lower laser head position G_L
$\left|\overrightarrow{G_L G}\right| = 5.3\text{mm}$

Figure 4.5. Different Center of Gravity Configurations above Point G (See Figure 2.4)

4.5. Test Setup and Procedure for Dynamic Performance Evaluation

In this section, in order to compare the trajectory tracking performances of the 2-DoF planar mechanisms test setup and procedure will be given. To observe the end-effector trajectory of the mechanism Haas PHF-25 fiber-optic laser head is chosen. In Figure 4.6, the lased head assembled mechanism with an adjustable work table and coated chipboard to observe the output paths of end-effector can be seen. For evaluation of the dynamic performances of these mechanisms, the output paths are subjected to some basic image processing algorithms to derive the dimensions and key features of paths.

These dynamic performance tests are executed for 8 different configurations. There are two different structural mechanisms which are 2-DoF over-constrained and 2-DoF simply-constrained mechanisms (See Figure 3.1), two different laser head positions introduced as upper laser head position G_U and lower laser head position G_L (See Figure 4.5), also, the last two different configurations are the mechanisms with compliance model algorithm or without compliance model algorithm. These 8 different configurations are subjected to the dynamic performance tests that measure the trajectory tracking ability up to 5 g accelerations with the defined three different motions which are x-motion, y-motion, and combined motion.

In Figure 4.7, these defined paths can be seen. The path in Figure 4.7a is defined

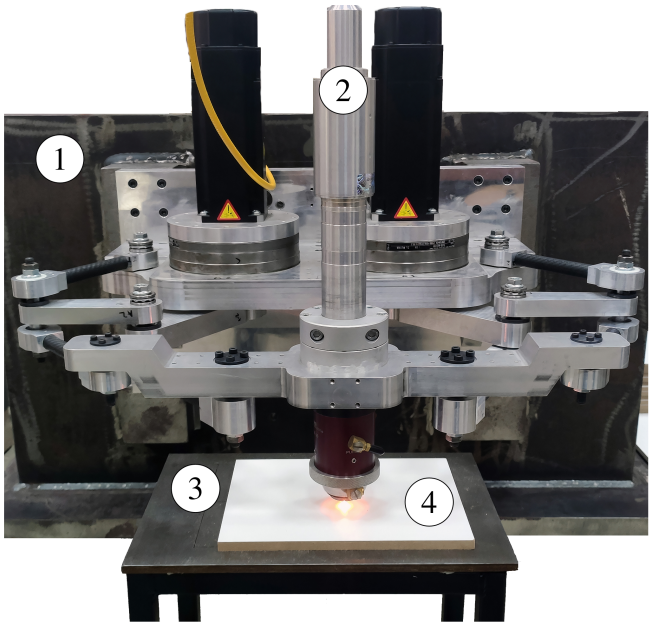

Figure 4.6. 2-DoF planar over-constrained mechanism: 1:Base, 2: PHF-25 Laser process head, 3: Adjustable work table, 4: Coated chipboard

for separate end-effector motions on the x and y-axis and its dimensions are limited with workspace dimensions. The path in Figure 4.7b is defined for combined end-effector motion and its dimensions are given randomly. The arrows sketched on the figures define the end-effector motion respectively.

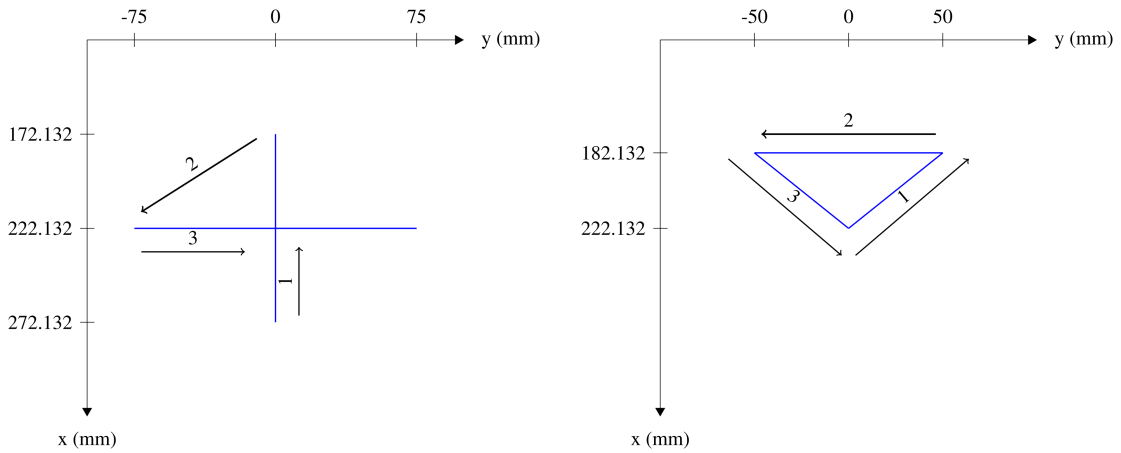

Figure 4.7. Defined paths for dynamic performance evaluation

4.6. Image Processing Algorithm

Image processing algorithm takes place in 6 steps;

i. By using a 1200 dpi scanner, output paths on the chipboard are scanned .

ii. Filtering process is done in order to get rid of noisy data.

iii. Coordinates of pixels related to the defined paths are found.

iv. Spline and line fitting processes are executed to these pixels by using the fit and polyfit functions in MATLAB.

v. Pixel coordinates are transformed to world coordinates by using the dpi information of the scanner.

vi. Key features like distance and total area under the fluctuations are calculated.

In order to verify the image processing algorithm, defined paths (Figure 4.7) are used. 100 mm length of x motion and 150 mm length of y motion calculated as 99.98 mm and 150.08 mm respectively.

In Figure 4.8, the outcome of the image processing algorithm can be seen for a sample laser marking operation conducted at 5 g acceleration.

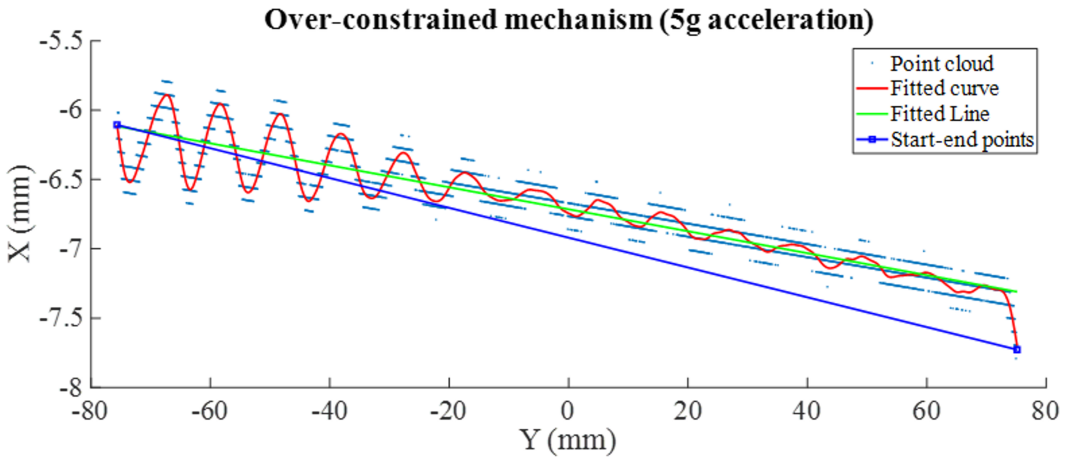

Figure 4.8. Image processing algorithm output

4.7. Test Results

For dynamic performance evaluation of the mechanisms, test setup and procedure are given in Section 4.5. The image processing procedure in order to collect data from the laser marked chipboards is given in Section 4.6. Length of motion has been measured

between the start and end-point of the trajectory. In order to express the deviation from linearity, the total area has been measured as the area between the fitted line and fitted spline. Because the image processing algorithm was not consistent to determine the corners correctly for the triangle motion, just the total area between the fitted spline and the fitted line is given by separating triangle images into the three lines. After performing image processing for all three lines, the total area is found by summing up the areas of each of these lines.

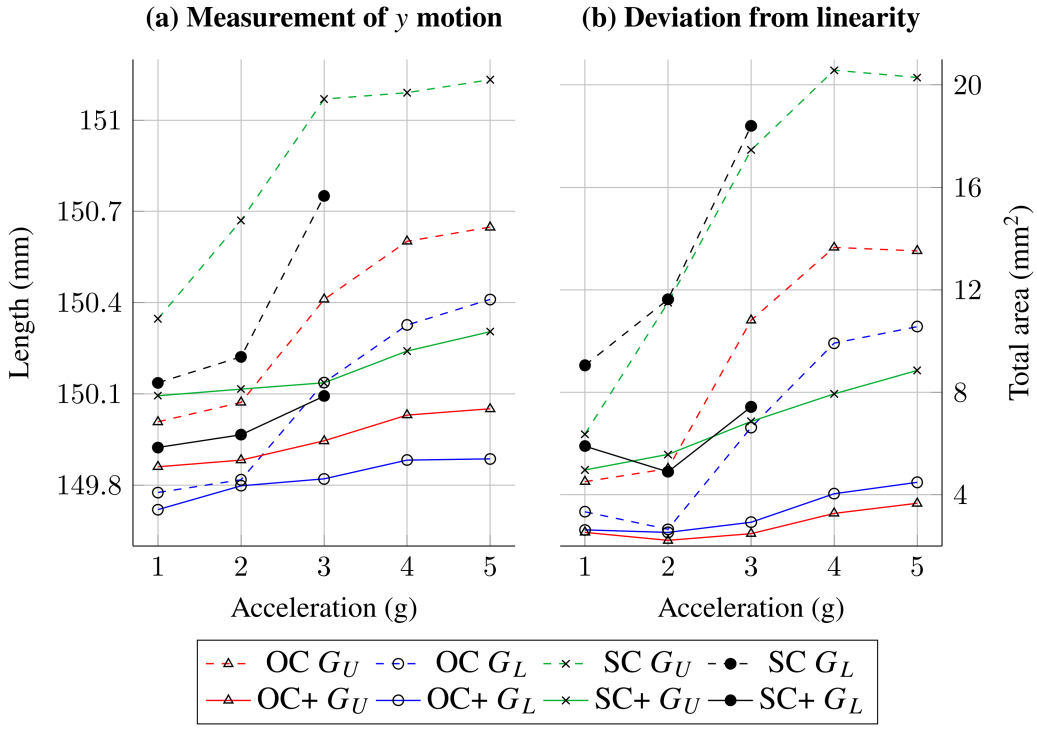

Figure 4.9. Trajectory following performance at the y-axis

In Figure 4.9, trajectory following performance at the y-axis is given. The motion is 150 mm of a straight line. In Figure 4.9a, the length measurement of the y motion with respect to the increasing accelerations from 1 g to 5 g is plotted. OC, SC, G_U, G_L and + stands for over-constrained, simply constrained, upper CG position, lower CG position and enabled compliance prediction algorithm respectively. Static calibration of the mechanism is executed at the OC G_U configuration. It can be seen that for that condition, the length of the straight line y motion has been measured around 150 mm at 1 g acceleration. While the maximum acceleration of the motion goes to 5 g, length measurement values go up to 150.7 mm due to the compliance of the mechanism. Because the calibration has been conducted only one condition, positioning accuracy changes with respect to the mechanism configuration. Therefore, absolute evaluation of length measurements does

not make sense. All different mechanism configurations should be evaluated relatively between the compliance modeled condition and without the compliance modeled condition for the length measurements. To make it clear, the same color and mark were used for this relative evaluation process.

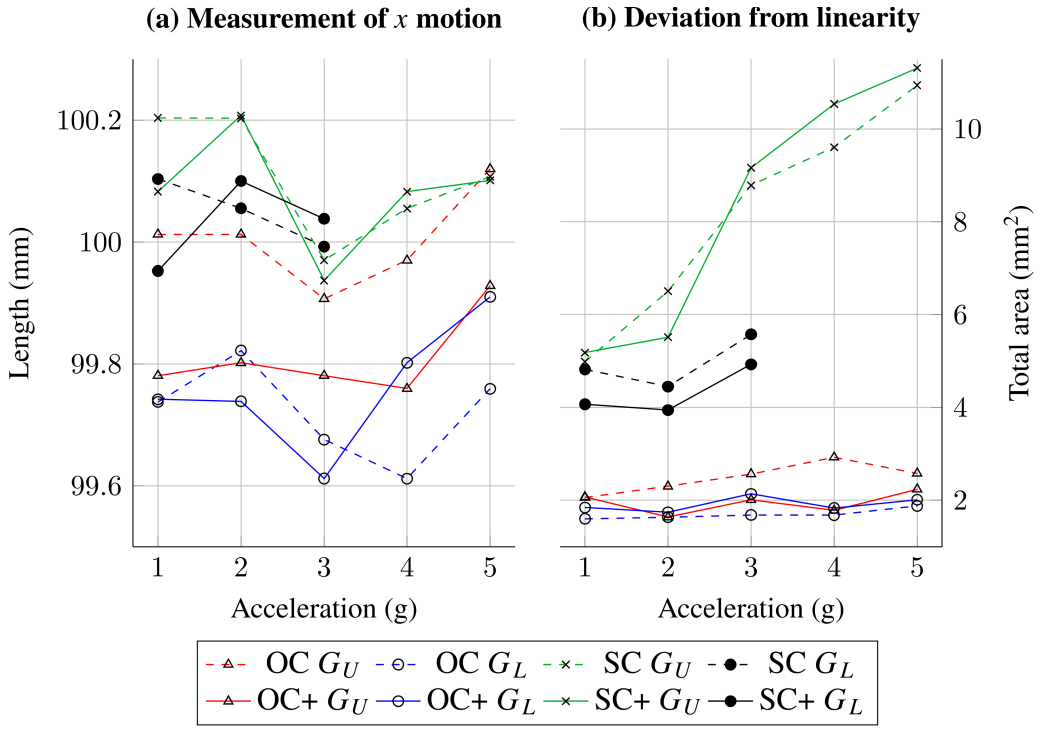

Figure 4.10. Trajectory following performance at the x-axis

For all configurations, the range of the length measurement of y motion is decreased to a lower valued-narrow range with the activation of the compliance prediction algorithm. Also, relatively lowering slopes of the compliance modeled configurations support this outcome. In Figure 4.9b, deviation from linearity is given. This time absolute evaluation can be done because it shows the vibrations along the vertical direction of the desired motion. Without a compliance prediction algorithm, OC G_L is the best performing configuration that eliminates vibration effects. With the compliance modeled versions of these mechanisms, OC+ G_U shows slightly better performance with respect to the OC+ G_L condition. There are 2 candidate reasons for this situation. One of them is, because the compliance models of both over-constrained mechanisms are the same, lowering compliance model gains might be beneficial for the OC+ G_L case. The other reason is the compliance model data arranged for the tip point of the end-effector position of the G_U position. Therefore, the compliance data might fit better to this condition.

In Figure 4.10, trajectory tracking performance along the x- axis is given. The in-

tended trajectory is 100 mm of a straight line. In Figure 4.10a, measurement of x motion is plotted. Here, the length measurements do not increase monotonically while the accelerations increase monotonically. Also, while the compliance prediction algorithm decreases length measurements for the OC G_U condition, OC G_L case has not been affected in the same way. For 2 and 3 g x motions, the length measurements of the motion increase while for the 4 and 5 g x motions, it decreases. Also, for simply-constrained configurations, no positive and consistent effect of the compliance prediction algorithm has not been observed. In Figure 4.10b, deviations from linearity for the x motion can be seen. It is clear that over-constrained configurations show better performance with respect to the simply-constrained configurations. Due to the symmetric structure of over-constrained configuration, no compliant displacements along the axis $y = 0$ are not expected. The same relationship that is seen for the y motion can be seen also for the x motion. This relation is without compliance prediction algorithm, OC G_L shows fewer deviations with respect to the OC G_U configuration. Although deviations for the over-constrained conditions take place in the small region between $[1.6, 3]$ mm^2, the best case is seen as OC G_L and the compliance prediction algorithm shows a negative effect that increases the deviations.

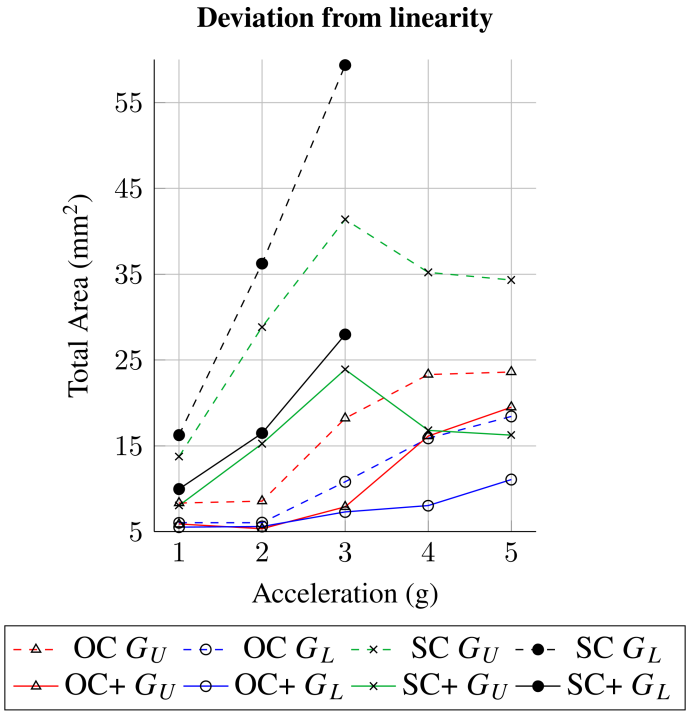

Figure 4.11. Trajectory following performance for the combined triangle motion

In Figure 4.11, the deviation from linearity in terms of the total area is given for

the combined triangle motion. The highest deviation is observed for the case SC+ G_L configuration at 3 g accelerations. While executing a laser marking test for this condition, there was a disturbing voice coming from the mechanism. Therefore, for the higher accelerations in this condition, laser marking tests are canceled. The line chart is so similar to the deviations for y motion. However, for the combined motion, the best case is observed as OC+ G_L while for the y motion, OC+ G_U shows slightly better performance.

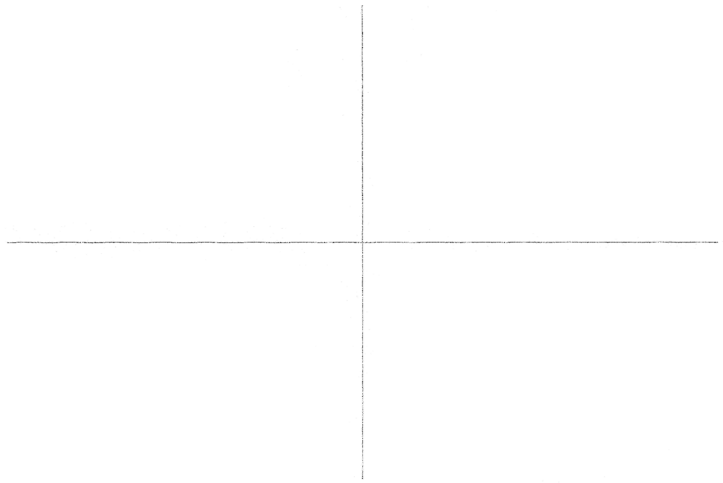

(a) 5g OC+ G_U

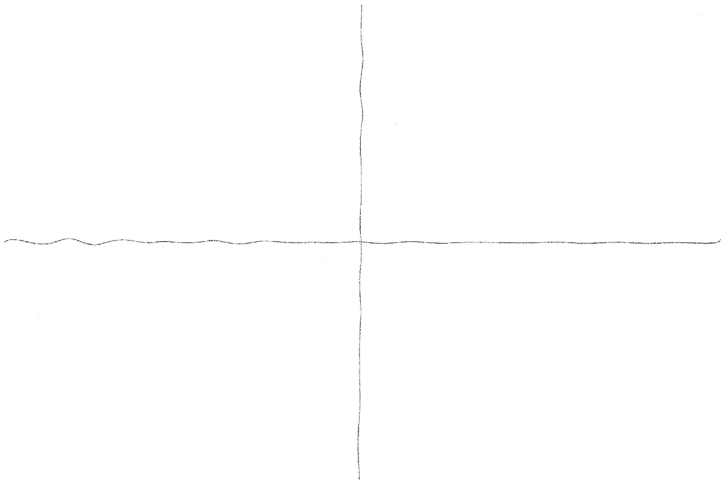

(b) 5g SC G_U

Figure 4.12. Illustrations of the worst and best cases for x and y motion

According to the total deviation from linearity results based on the image processing algorithm, the best and worst cases are illustrated below. In Figure 4.12, the cases for the x and y motions, and in Figure 4.13, the cases for the combined motion can be

seen. If we look carefully at the worst cases, it can be said that the vibrations start at the beginning of the motions and then damps. Also, the end-effector of the mechanism wants to change its direction at the finishing of the straight line. However, because of the energy storing and releasing situation or it can be interpreted as compliance of the mechanism, the corners at the laser marked paths of the motions includes imperfections.

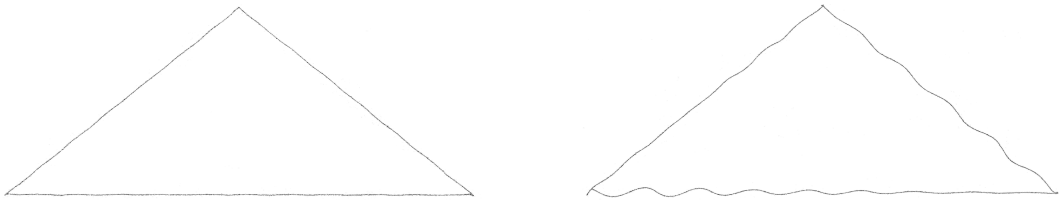

(a) 5g OC+ G_L (b) 3g SC G_L

Figure 4.13. Illustrations of the worst and best cases for combined motion

4.8. Summary

As a consequence of this chapter, the simple data-driven compliance algorithm is generated for the over-constrained and simply-constrained mechanisms via making some logical assumptions and using the D'Alembert principle while passing to dynamic condition. The hardware setup and flowchart diagram for updating trajectory by using the compliance model of the mechanisms is given. In order to observe the output trajectory of the end-effector, a laser head is assembled to end-effector of the mechanism. In order to evaluate the effect of the CG position of the mechanism and the compliance prediction algorithm, 8 different configurations are determined. After that, for dynamic performance tests, test setup and procedure are given and to evaluate the output trajectories on the chipboards, the image processing algorithm has been introduced briefly. According to the test results, it can be said that without a compliance prediction algorithm, the general best performer is the OC G_L configurations. Usually, the compliance prediction algorithm affects all conditions positively. OC+ configurations for the y motions show similar performance in the small deviation range while in the combined motion, it is clear that the vibrations tolerated better in the OC+ G_L configuration.

CHAPTER 5

CONCLUSION

As a conclusion, the findings and outcomes of the thesis are presented in the following:

i. It is shown that the center of gravity of the end-effector and the joint types affect the trajectory tracking accuracy of the mechanism.

ii. Over-constrained mechanism presents better trajectory tracking performance than simply-constrained mechanism.

iii. Data-driven compliance prediction algorithm enhances the trajectory tracking performance of the mechanisms.

The following statements can be taken into consideration to enhance the trajectory tracking performance of the mechanism more:

i. The location of the optimal center of gravity of the end-effector can be found experimentally. The term is to be determined that the location of the CG of the mechanism along the z-axis. By using the compliance measurement process executed in Chapter 2, forcing at five different locations specified along the z direction can be applied along the x- and y-axis. After that, polynomial interpolation with a quadratic curve fitting can be used to find the z position of the CG of the mechanism where the bending compliant displacements are minimum.

ii. In the OC mechanism, there are four spherical roller bearings that affect the end-effector positioning accuracy. The number of spherical roller bearings can be decreased by changing them with ball bearings. The process can be done by observing the torque values of the actuators in the dynamic condition, by decreasing the number of spherical roller bearing one by one.

iii. Symmetric design of the mechanism with respect to a xy- plane that includes the center of gravity of the mechanism might be a solution.

After enhancing the compliance behavior of the mechanism mechanically, rigid body kinematics while estimating the D'Alembert forces will work more accurately. Also, if the positional deviations calculated from the rigid body kinematics decreases, the compliance prediction algorithm will work better because the compliance prediction algorithm estimates the compliances with respect to the rigid body kinematics. When the compliances and nonlinearities decrease, the algorithm and actuators can respond better.

REFERENCES

Alici, G. and B. Shirinzadeh (2005). Enhanced stiffness modeling, identification and characterization for robot manipulators. *IEEE transactions on robotics 21*(4), 554–564.

Bern, J. M., Y. Schnider, P. Banzet, N. Kumar, and S. Coros (2020). Soft robot control with a learned differentiable model. In *2020 3rd IEEE International Conference on Soft Robotics (RoboSoft)*, pp. 417–423. IEEE.

Ceccarelli, M. and G. Carbone (2005). Numerical and experimental analysis of the stiffness performances of parallel manipulators. In *2nd international colloquium collaborative research centre*, Volume 562, pp. 21–35. Citeseer.

Conrad, K. L., P. S. Shiakolas, and T. Yih (2000). Robotic calibration issues: Accuracy, repeatability and calibration. In *Proceedings of the 8th Mediterranean Conference on Control and Automation (MED2000), Rio, Patras, Greece*, Volume 1719.

Dede, M. İ. C., G. Kiper, and E. Uzunoğlu (2016). A macro-micro mechanism design for laser cutting process.

Gogu, G. (2005). Mobility of mechanisms: a critical review. *Mechanism and Machine Theory 40*(9), 1068–1097.

Kiper, G., M. İ. C. Dede, E. Uzunoğlu, and E. Mastar (2015). Use of hidden robot concept for calibration of an over-constrained mechanism.

Klimchik, A. (2011). *Enhanced stiffness modeling of serial and parallel manipulators for robotic-based processing of high performance materials*. Ph. D. thesis, Ecole Centrale de Nantes (ECN); Ecole des Mines de Nantes.

Klimchik, A., D. Bondarenko, A. Pashkevich, S. Briot, and B. Furet (2014). Compliance error compensation in robotic-based milling. In *Informatics in control, automation and robotics*, pp. 197–216. Springer.

Merlet, J.-P. and C. Gosselin (2008). Parallel mechanisms and robots.

Özkahya, M. (2019). Design and experimental evaluation of a dynamically balanced overconstrained planar 6r parallel manipulator. Master's thesis, Izmir Institute of Technology.

Patel, Y., P. George, et al. (2012). Parallel manipulators applications—a survey. *Modern Mechanical Engineering 2*(03), 57.

Taner, B. and M. İ. C. Dede (2017). Image processing based stiffness mapping of a haptic device. In *New Advances in Mechanisms, Mechanical Transmissions and Robotics*, pp. 447–454. Springer.

Uzunoğlu, E. (2019). Macro-micro robotic manipulation: A laser cutting case study.